

Chrome-spinel in Hayabusa particles: Recorders of Asteroid Itokawa's thermal history

Jemma Davidson^{1,2}, Devin L. Schrader^{1,2}, Thomas J. Zega³, Pierre Haenecour³, Kenneth J. Domanik³, Kazuhide Nagashima⁴, Noriko Kita⁵ and Philipp Heck^{6,7}.

¹*Buseck Center for Meteorite Studies, Arizona State University, AZ 85287, USA*

²*School for Earth and Space Exploration, Arizona State University, AZ 85287, USA*

³*Lunar and Planetary Laboratory, University of Arizona, AZ 85721, USA*

⁴*Hawai'i Institute of Geophysics and Planetology, University of Hawai'i at Mānoa, HI 96822 USA*

⁵*WiscSIMS, University of Wisconsin-Madison, Madison WI 53706, USA*

⁶*Robert A. Pritzker Center of Meteoritics and Polar Studies, Negaunee Integrative Research Center, Field Museum of Natural History, Chicago, IL 60605, USA*

⁷*Department of the Geophysical Sciences, University of Chicago, Chicago, IL, USA*

Introduction: Chrome-spinel, which includes chromite (FeCr_2O_4) and Cr-rich spinel ($[\text{Mg,Fe}][\text{Al,Cr}]_2\text{O}_4$), records both pre- and post-accretionary formation conditions while remaining resilient to extensive alteration (e.g., [1–5]). They are found in a wide variety of astromaterials, including chondrites, as well as Hayabusa [6] and Stardust [5] returned samples. The morphologies, chemical compositions, and O-isotope compositions of chrome-spinel minerals in returned samples provide important information on their primary formation conditions in the nebula (temperature, time, oxygen fugacity) and on the secondary alteration conditions on the parent body (thermal metamorphism).

Chrome-spinel and olivine in FeO-rich chondrules in carbonaceous and ordinary chondrites are very sensitive indicators of thermal metamorphism [1,4]. We compare the compositions, textures, and O-isotope compositions of chrome-spinel from asteroid 25143 Itokawa with those from ordinary chondrites to investigate correlations between formation mechanism, oxygen fugacity, and formation/alteration temperatures. Studying chrome-spinel in Hayabusa particles constrains the parent body formation and alteration conditions of asteroid 25143 Itokawa and provides information about the variety of material present on this asteroid (e.g., [6]).

Samples and analytical procedures: We were allocated three Hayabusa-returned particles during the Hayabusa AO7 (Table 1; Fig. 1a–c). Two of the allocated samples contain olivine-chrome-spinel pairs, while the third is solely chrome-spinel. All samples are large enough for multiple *in situ* O-isotope analyses.

Table 1. Hayabusa-returned samples for study.

Sample	Size (diameter)	Phases
RA-QD02-0316	117 × 51.5 μm	olivine, chr
RB-CV-0091	29.88 × 14 μm	olivine, chr
RB-CV-0262	39.2 × 23.3 μm	chr

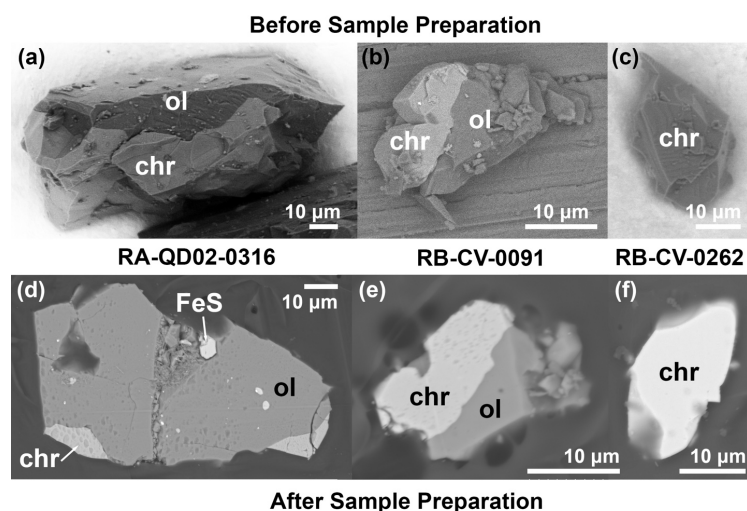


Figure 1. Hayabusa particles studied here (a, b, c) before, and (d, e, f) after sample preparation (i.e., mounting in epoxy and microtoming). (a–c) Backscattered electron (BSE) images modified from the JAXA Hayabusa particle catalogue used for preliminary identification of phases. (d–f) BSE images showing flat surfaces created by microtoming after mounting in epoxy. The orientation of RA-QD02-0316 changed slightly after mounting in epoxy, resulting in a smaller area of exposed spinel. Where chr = chrome-spinel, ol = olivine, and FeS = iron sulfide.

Sample preparation: The Itokawa samples were prepared at the University of Arizona's Lunar and Planetary Laboratory (LPL) following a modified version of the method presented in [7]: the particles were mounted on the top of epoxy bullets, which were then trimmed and sliced using a Leica EM UC7 ultramicrotome with two diamond knives (a trim knife and a cutting knife) to create flat surfaces that were suitable for microbeam analysis. The progressive excavation of each Itokawa grain was monitored using a Keyence VHX-7000 4K digital-optical microscope at LPL to ensure that overlying epoxy was removed to reveal

sufficient sample area for further analysis while preserving as much of the particle as possible. Analysis in 3D microscopy mode confirmed that the microtome method created smooth, flat surfaces ideal for EPMA and *in situ* O-isotope analysis.

Electron microscopy: The prepared samples were then carbon-coated and imaged in backscattered electron (BSE) mode in a Hitachi TM4000Plus II Tabletop scanning-electron microscope (SEM) at LPL Kuiper-Arizona Laboratory for Astromaterials Analysis facility (K-ALFAA) to verify that the microtome method created smooth, flat surfaces required for subsequent microprobe analysis (Fig. 1d–f). We then determined the major and minor element compositions of olivine and chrome-spinel in each of the Itokawa particles using the Cameca SX-100 EPMA at LPL K-ALFAA.

Results: Olivine-spinel thermometry: The olivine-spinel geothermometer was used to calculate closure temperatures for the two Itokawa particles that contain olivine and chrome-spinel mineral pairs (RA-QD02-0316 and RB-CV-0091). Quantitative compositional analyses were performed via EPMA at the edges of mineral pairs to determine the major and minor element compositions of both phases. Olivine-spinel temperatures were then determined using these data and an Excel version of the MELTS calculator [9]. Temperatures were determined at a pressure of 1 bar, which is a reasonable approximation for asteroids [10]. These calculations yielded closure temperatures of $\sim 610 \pm 50$ °C (1 sigma, 1σ) to $\sim 710 \pm 50$ °C for the different particles, which agree within a 2σ error. Assuming the olivine and spinel pairs in Itokawa particles originated from chondrules, these temperatures do not reflect the conditions of chondrule crystallization but rather closure temperatures after thermal metamorphism (e.g., [11]), consistent with temperatures recorded by olivine-spinel pairs in LL3.5–6 chondrites [8]. Temperatures indicative of crystallization in the chondrules of LL3.00–3.3 chondrites are typically >1000 °C [8].

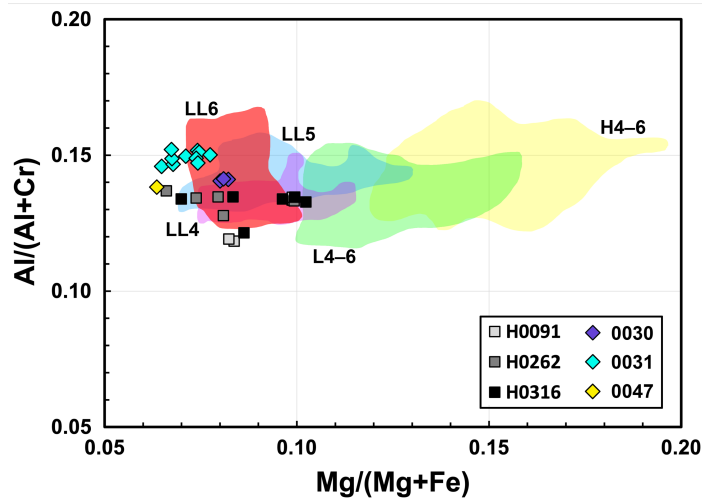


Figure 2. Chromite compositions for Hayabusa particles studied here (H0091, H0262, and H0316; squares) and from [6] (RA-QD02-0030, -0031, and -0047; diamonds) compared to those from ordinary chondrites (fields drawn from data in [6] and [8]).

Major and minor element compositions: The major and minor element compositions of each of the Itokawa chrome-spinels show that they have $\text{Cr}/(\text{Cr}+\text{Al}) > 0.8$, indicating that they are all chromite (i.e., FeCr_2O_4). Their $\text{Mg}/(\text{Mg}+\text{Fe})$ and $\text{Al}/(\text{Al}+\text{Cr})$ ratios cover a broader range than chromite compositions reported from three other Itokawa particles (RA-QD02-0030, -0031, and -0047) [6] (Fig. 2).

Since olivine-spinel geothermometry indicates that the Itokawa chromites studied here originate from thermally metamorphosed material, their compositions are compared with those from type 4–6 ordinary chondrites (LL, L, and H) (Fig. 2). The Itokawa chromites appear to be slightly less equilibrated than those previously reported by [6], which best match LL5 and LL6 chondrites, and cover similar compositions to chromites from LL4–6 chondrites (see comparison of OC data from [8] in Fig. 2).

Discussion: Due to the significant overlap between the major and minor element compositions of chromite from LL4–6 chondrites, it is not possible to match the Itokawa chromites studied here with specific petrologic types. Future work will include performing *in situ* O-isotope analyses of both olivine and chrome-spinel phases in each sample. This will enable us to constrain the specific meteorite petrologic type matches to the Itokawa chromites. However, the presence of Itokawa chromites covering the same range as LL4–6 chondrites is consistent with Itokawa being a breccia of LL4–6 materials [6].

References: [1] Johnson and Prinz 1991. *Geochimica et Cosmochimica Acta* 55:893–904. [2] Krot et al. 1993. *Earth & Planetary Science Letters* 119:569–584. [3] Kimura et al. 2006. *Geochimica et Cosmochimica Acta* 70:5634–5650. [4] Davidson et al. 2011. Abstract #5319. *Meteoritics & Planetary Science Supplement*. [5] Gainsforth et al. 2015. *Meteoritics & Planetary Science* 50:976–1004. [6] Nakamura et al. 2011. *Science* 333:1113–1116. [7] Che and Zega 2023. *Nature Astronomy* DOI:10.1038/s41550-023-02012-x. [8] Kimura et al. 2006. *Geochimica et Cosmochimica Acta* 70:5634–5650. [9] Sack and Ghiorso 1991. *American Mineralogist* 76:827–847. [10] Benedix et al. 2005. *Geochimica et Cosmochimica Acta* 69:5123–5131. [11] Wlotzka 2005. *Meteoritics & Planetary Science* 40:1673–1702.

Coordinated Analyses of Hayabusa particles RB-CV-0234, RB-QD04-0039, and RA-QD02-0310: Constraints on asteroid Itokawa formation from sulfides and silicates

Devin L. Schrader¹ and Thomas J. Zega²

¹*Buseck Center for Meteorite Studies, School of Earth and Space Exploration, Arizona State University, Tempe, AZ 85287-1404, USA (devin.schrader@asu.edu),*

²*Lunar and Planetary Laboratory, University of Arizona, Tucson, Arizona 85721, USA (tzega@arizona.edu)*

Introduction: Sulfides are important phases in planetary materials because their compositions, textures, and crystal structures can be used to constrain oxygen fugacity of formation, shock stage, and aqueous-, thermal-, and cooling-histories [e.g., 1–8]. The pyrrhotite-group sulfides are largely nonstoichiometric and have a range of compositions (typically $0 \leq x \leq 0.125$, but x can be ≤ 0.2 ; i.e., FeS [troilite] to $\text{Fe}_{0.8}\text{S}$) and distinct crystal structures (polytypes). The stoichiometric end members are 2C (troilite; FeS, hexagonal) and typically 4C (Fe_7S_8 , monoclinic) pyrrhotite. There are also pyrrhotites of intermediate compositions with $0 \leq x \leq 0.2$ (all hexagonal), including the non-integral NC-pyrrhotites and the integral 5C (Fe_9S_{10}), 6C ($\text{Fe}_{11}\text{S}_{12}$), and 11C ($\text{Fe}_{10}\text{S}_{11}$) pyrrhotites [e.g., 9–11]. Geothermometry of pyrrhotite-pentlandite intergrowths in meteorites shows that most formed via primary cooling from high temperature (i.e., chondrule cooling in the protoplanetary disk) or thermal alteration on the parent body [e.g., 12–14]. Sulfides in the LL4 to LL6 chondrites typically equilibrated $\leq 230^\circ\text{C}$, consistent with formation during cooling after thermal metamorphism [2]. Analyses of Hayabusa particles identified asteroid 25143 Itokawa as LL4–6 chondrite material ($\sim 10\%$ LL4 and $\sim 90\%$ LL5–6) [e.g., 15–18] that was thermally metamorphosed between ~ 780 and 840°C [15]. Itokawa particles were found to record shock stages between S2 and S4, with most particles around S2 [19,20]. Sulfides in Hayabusa particles [e.g., 15,21,22] may record additional and/or complementary information on the formation conditions of asteroid Itokawa.

We performed coordinated analyses of the Hayabusa particles RB-CV-0234, RB-QD04-0039, and RA-QD02-0310, allocated in Hayabusa AO5. Preliminary analysis by JAXA's Hayabusa examination team via scanning electron microscopy (SEM) determined that particle RB-CV-0234 (25.9 μm in diameter) consists of FeS, Fe, FeNiS, and CuS, making it an ideal target potentially containing both pyrrhotite group sulfides [$(\text{Fe},\text{Ni},\text{Co},\text{Cr})_{1-x}\text{S}$] and the rare Ni-rich sulfide, pentlandite [$(\text{Fe},\text{Ni},\text{Co},\text{Cr})_9\text{S}_8$]. In addition, JAXA's Hayabusa examination team determined that particle RB-QD04-0039 (52 μm in diameter) consists of olivine, low-calcium pyroxene, and troilite, and that particle RA-QD02-0310 (127 μm in diameter) consists of olivine, plagioclase, and troilite. These two Hayabusa particles provided excellent opportunities to identify sulfides with petrographic context and to analyze their adjoining silicate minerals, unlike RB-CV-0234 that only contained sulfides. Here, we compared in situ analyses of these particles to the results from LL3–6 chondrite silicates and sulfides [e.g., 1,2], with the goal of further constraining the formation and alteration conditions of asteroid Itokawa. Preliminary analyses from RB-CV-0234 and RB-QD04-0039 were presented in [23,24,25].

Samples and Analytical Procedures: We mounted RB-CV-0234, RB-QD04-0039, and RA-QD02-0310 each on epoxy bullets, using a method modified from [21], and microtomed them in preparation for analysis and sample extraction using the FEI Helios NanoLab 660 focused-ion-beam-SEM (FIB-SEM) at the University of Arizona (UAz). X-ray element maps and high-resolution images of the microtomed RB-CV-0234 and RB-QD04-0039 were obtained with the FIB-SEM prior to extraction of a $\sim 10 \times 10 \mu\text{m}$ sections from each particle, which were then thinned to electron transparency ($< 100 \text{ nm}$) following the methods of [26]. The FIB sections were then analyzed using the 200 keV aberration-corrected Hitachi HF5000 scanning transmission electron microscope (S/TEM) at UAz. After a FIB section of the sulfide from RB-QD04-0039 was obtained, RB-QD04-0039 was analyzed on the Cameca SX-100 electron microprobe (EPMA) at UAz. Microtome preparation of RA-QD02-0310 did not reveal sulfides for further structural analyses via TEM, but the compositions of its silicates were determined via EPMA at UAz.

Results: FIB-SEM X-ray element maps showed that the microtomed surface of RB-CV-0234 consisted entirely of pyrrhotite. However, X-ray element maps of the extracted FIB section, determined via TEM analysis, revealed a single large grain of pyrrhotite and a single smaller grain of pentlandite ($4.8 \times 1.3 \mu\text{m}$) at the bottom of the section (**Fig. 1**). Selected-area electron-diffraction (SAED) patterns of the pyrrhotite and pentlandite grains index to 2C pyrrhotite (troilite) and pentlandite along the [110] zone axis (i.e., they are crystallographically oriented), respectively. The compositions of RB-CV-0234 via quantitative

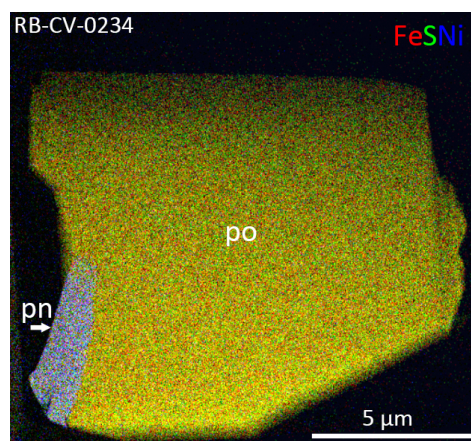


Figure 1. Composite TEM X-ray element map (RGB=FeSNI) of RB-CV-0234 FIB Section; where po = pyrrhotite and pn = pentlandite.

energy-dispersive X-ray spectroscopy [27] are 35.2 wt.% S and 64.8 wt.% Fe for pyrrhotite, and 32.4 wt.% S, 49.4 wt.% Fe, and 18.2 wt.% Ni for pentlandite. The microtomed surface of RB-QD04-0039 showed a single sulfide grain, as well as olivine (Fa28.1–29.5, Fa28.9±0.5 [1 σ]; n = 7) and low-calcium pyroxene (Fs23.8–24.9, Fs24.3±0.6, Wo1.1±0.1 [1 σ]; n = 3) (**Fig. 2**). A FIB section of the sulfide grain in RB-QD04-0039 revealed it to be troilite. The microtomed surface of RA-QD02-0310 showed a grain of olivine (Fa28.9–31.3, Fa30.2±0.8 [1 σ]; n = 12), with two chrome-spinels.

Discussion: The sulfides in RB-CV-0234 are most consistent with it being a sulfide grain from an LL6 chondrite, similar to the sulfides from Saint-Séverin studied by [1,2]. We infer this because: (1) the Ni content of pentlandite is consistent with the characteristic Ni contents of LL chondrite pentlandite [2,14]; and (2) based on results from the LL3–6 chondrite sulfides we previously studied [1,2,14], sulfide grains in Saint-Séverin (LL6, S2 [2,28]) contain a similar pentlandite/pyrrhotite morphology (i.e., blocky pentlandite in pyrrhotite) and 2C pyrrhotite (troilite) with pentlandite [1]. The other LL chondrites we studied contained either a distinct morphology (e.g., pentlandite lamellae) and/or multiple polytypes of pyrrhotite [1,2]. The compositions of pyrrhotite and pentlandite in RB-CV-0234 are consistent with equilibrating <300°C, perhaps as low as 230°C, similar to that of LL4–6 chondrites [2,25]. The olivine grain in RB-QD04-0039 contains planar fractures, indicating a shock stage of at least S3 and minimum shock pressures of 5–10 GPa [29]. The silicate compositions of both RB-QD04-0039 and RA-QD02-0310 (Fa28.9±0.5 and Fa30.2±0.8, respectively) are consistent with that of equilibrated LL chondrites, consistent with that found by [15] for Hayabusa particles. Relative to the iron-wüstite (IW) buffer, the oxygen fugacity constraints on the formation of troilite [30] and of pentlandite [14] indicates that RB-CV-0234 and RB-QD04-0039 were likely altered between approximately IW–2.2 and IW, consistent with that found for LL5 and LL6 chondrites by [14]. Therefore, the morphology and chemical compositions of sulfides and silicates of RB-CV-0234, RB-QD04-0039, and RA-QD02-0310, as well as inferred sulfide equilibration temperature and oxygen fugacity constraints are consistent with equilibrated LL chondrites.

Acknowledgements: We thank JAXA for the loan of the Hayabusa particles used in this study through the 5th International Announcement of Opportunity, and NASA grant NNX17AE53G (DLS PI, TJZ Co-I) for funding this research.

References

- [1] Schrader D. L. and Zega T. J. 2017. Abstract #6347. 80th MetSoc. [2] Schrader D. L. and Zega T. J. 2019. *Geochim. Cosmochim. Acta* 264:165. [3] Arnold R. G. 1967. *Can. Min.* 9:31. [4] Kissin S. A. and Scott S. D. 1982. *Econ. Geol.* 77:1739. [5] Raghavan V. 2004. *J. Phase Equilib.* 25:373. [6] Wang H. et al. 2006. *J. Sulfur Chem.* 27:1. [7] Harries D. and Langenhorst F. 2013. *Meteorit. Planet. Sci.* 48:879. [8] Bennet M. E. and McSween Jr. H. Y. 1996. *Meteorit. Planet. Sci.* 31:255. [9] Morimoto N. et al. 1975. *Econ. Geo.* 70:824. [10] Wang H. et al. 2006. *J. Sulfur Chem.* 27:1. [11] Harries D. et al. 2011. *Am. Min.* 96:716. [12] Jamsja N. and Ruzicka A. 2010. *Meteorit. Planet. Sci.* 45:828. [13] Schrader D. L. et al. 2015. *Meteorit. Planet. Sci.* 50:15. [14] Nakamura T. et al. 2011. *Science* 333:1113. [15] Schrader D. L. et al. 2016. *Geochim. Cosmochim. Acta* 189:359. [16] Noguchi T. et al. 2014. *Earth, Planets, and Space* 66:124. [17] Tsuchiyama A. et al. 2011. *Science* 333: 1125. [18] Tsuchiyama A. et al. 2014. *Meteorit. Planet. Sci.* 49:172. [19] Noguchi T. et al. 2011. *Science* 333:1121. [20] Zolensky M. E. et al. 2012. Abstract #1477. 43rd LPSC. [21] Berger E. L. and Keller L. P. 2015. *Microscopy Today* 23:18. [22] Harries D. and Langenhorst F. 2014. *Earth, Planets, and Space* 66:163. [23] Schrader D. L. and Zega T. J. 2018. *Hayabusa 2018, 6th Symposium on Solar System Materials*. [24] Schrader D. L. and Zega T. J. 2019a. *Lunar Planet. Sci. L*, Lunar Planet. Inst., Houston, #2009. [25] Schrader D. L. and Zega T. J. 2019b. Abstract #6400. 82nd MetSoc. [26] Zega T. J. et al. 2007. *Meteorit. Planet. Sci.* 42:1373. [27] Zega T. J. et al. 2018. Abstract #2084. *Microsc. Microanal.* 24 (Suppl. 1). [28] Rubin A. E. 2004. *Geochim. Cosmochim. Acta* 68:673. [29] Stöffler D. et al. 2018. *Meteorit. Planet. Sci.* 53:5. [30] Schrader D. L. et al. 2021. *Geochim. Cosmochim. Acta* 303:66.

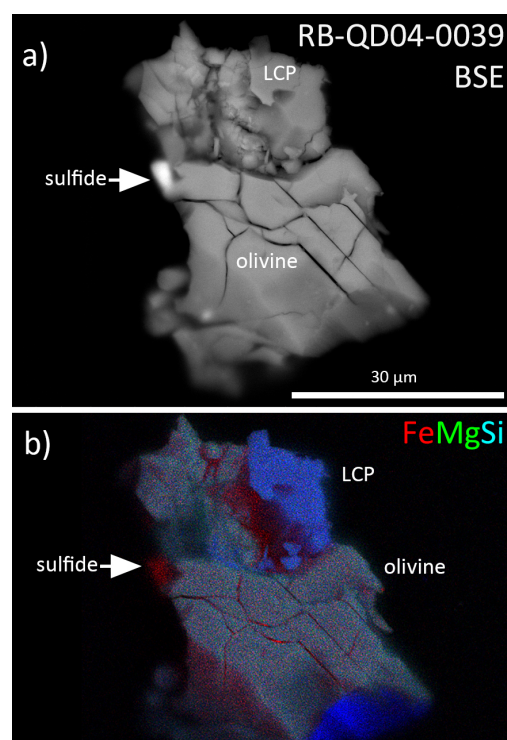


Figure 2. (a) Back scattered electron (BSE) image and composite EPMA X-ray element map (RGB=FeMgSi) of RB-QD04-0039; LCP = low-calcium pyroxene.

Are there 100s of ppm water in nominally anhydrous minerals of non-carbonaceous asteroids?

Dennis Harries¹

¹*European Space Resources Innovation Centre (ESRIC), Luxembourg Institute of Science and Technology, 41 rue du Brill, L-4422 Belvaux, Luxembourg*

Non-carbonaceous (NC) asteroids of mainly the S type comprise a large fraction of objects in the main asteroid belt and among the near-Earth asteroid population. Materials represented by them have played significant roles in the accretion of the terrestrial planets, but generally NC materials have been considered essentially dry relative to carbonaceous chondrites (CC). In consequence, NC planetesimals were usually not considered as carriers of H₂O delivered to the early Earth. Recently, SIMS studies of regolith particles returned by JAXA's Hayabusa mission from S-type/LL-group asteroid 25143 Itokawa have reported 240 to 990 ppm H₂O in the nominally anhydrous minerals (NAMs) orthopyroxene, olivine, and albite [1,2]. Additional data has indicated similar contents in NAMs of equilibrated chondrites of the L and LL groups [1,3] and in NAMs of unequilibrated chondrites [4].

H₂O contents on the order of 100s of ppm in NAMs of ordinary chondrites would have substantial implications for the early accretion of H₂O to the proto-Earth and would also imply high lithostatic pressures during thermometamorphism within chondritic planetesimals not consistent with current size estimates. Moreover, high water-to-rock ratios during metamorphism could indicate much higher bulk H₂O contents of pristine equilibrated chondrites beyond the defect-bound hydroxyl component, e.g., in the form of fluid inclusions. This would have considerable implications for the targeting of S-type near-Earth asteroids for in-situ space resources utilization (ISRU).

In order to shed more light on the H₂O contents in asteroidal NAMs, we have conducted a survey of H₂O in equilibrated chondrites and achondrites using the NanoSIMS 50L at the Open University, UK [5]. This contribution serves to place these results in perspective with other recent findings. The NAMs studied comprise olivine and orthopyroxene from a set of equilibrated ordinary chondrites of the L and LL groups (Baszkówka, Bensour, Kheneg Ljouâd, and Tuxtuac) and several ultramafic achondrites (Zakłodzie, Dhofar 125, Northwest Africa [NWA] 4969, NWA 6693, and NWA 7317). For calibration we used terrestrial olivine and orthopyroxene with H₂O contents determined by Fourier transform infrared spectroscopy. Our 99.7% (~3SD) detection limits achieved were 3.6 to 5.4 ppm H₂O for olivine and 7.7 to 10.9 ppm H₂O for orthopyroxene.

Our survey did not identify any meteorite sample that consistently showed H₂O contents in NAMs above our detection limits. Other recent SIMS studies of H₂O in NAMs of ungrouped achondrites and acapulcoites/lodranites, including NWA 6704 (paired with our sample of NWA 6693) and Dhofar 125, did not detect H₂O above 2.1 ppm [6] and 6.6 ppm [7], respectively. SIMS analyses of NAMs in unequilibrated chondrites by have also indicated very low H₂O contents of 8 to 14 ppm in these materials [8].

Finding H₂O contents one to two orders of magnitude lower than previously reported suggests that the parent planetesimals of the highly metamorphic chondrites, primitive achondrites and ultramafic achondrites studied were efficiently degassed during metamorphism and melting, if they initially had held substantial amounts of volatiles [5,6]. The discrepancies between SIMS analyses of Itokawa samples/equilibrated chondrites showing 100s of ppm H₂O on the one hand and equilibrated chondrites showing hardly any detectable H₂O on the other hand may stem from two contributions: Systematic errors of the analyses and/or heterogeneity of the samples. Sample contamination leading to systematically biased H₂O contents is a major suspect. It appears more likely to occur than H₂O loss from the strongly bound hydroxyl defects in NAMs, which requires substantial or prolonged heating to diffusively remove H₂O. The studies available rarely analysed the same samples or meteorites, rendering it difficult to rule out sample heterogeneity. However, there is currently no other indication to support the hypothesis that common equilibrated chondrites underwent metamorphism under vastly different peak pressures and H₂O fugacities, leading to heterogeneous H₂O contents in NAMs among different meteorites.

Hence, the presence of 100s of ppm H₂O in samples of asteroid Itokawa and equilibrated non-carbonaceous chondrites is doubtful and the role of their parent bodies in delivering water to the terrestrial planets needs to be questioned.

References

- [1] Jin Z. and Bose M. 2019. *Science Advances* 5:eaav8106.
- [2] Chan Q.H.S. et al. 2021. *Scientific Reports* 11:5125.
- [3] Jin Z. et al. 2021. *Planetary Science Journal* 2:244.
- [4] Stephant A. et al. 2017. *Geochimica et Cosmochimica Acta* 199:75–90.
- [5] Harries D. et al. 2023. *Meteoritics & Planetary Science* 58:705–721.
- [6] Newcombe M.E. et al. 2023. *Nature* 615:854–857.
- [7] Stephant A. et al. 2023. *Earth and Planetary Science Letters* 615:118202.
- [8] Shimizu K. et al. 2021. *Geochimica et Cosmochimica Acta* 301:230–258.

Development of Nondestructive X-ray CT Imaging Techniques to Identify and Locate Presolar Grains in Meteorite Sample Jbilet with Application to Ryugu Samples

D. Z. Shulaker¹, M. Ferrucci², B. M. Rogers², M. R. Savina¹, B. H. Isselhardt¹, Q. Shollenberger¹

¹*Nuclear and Chemical Sciences Division, Lawrence Livermore National Laboratory, CA (shulaker1@llnl.gov)*

²*Materials Engineering Division, Lawrence Livermore National Laboratory, CA.*

Introduction: The development of non-destructive analytical methods of precious material from sample-return missions is necessary to preserve as much material as possible, including presolar grains. Most commonly, an entire sample is dissolved to isolate presolar grains from the sample matrix. However, dissolving an entire meteorite or material from a sample-return mission also dissolves essentially everything but presolar SiC, graphite, and nanodiamonds. This results in the loss of precious material and presolar silicates. In attempt to save sample material, previous studies target presolar graphite and silicon carbide (SiC) grains using nanoscale secondary ion mass spectrometry (NanoSIMS), scanning electron microscopy (SEM), and/or focused ion beam (FIB) to image regions of meteorite fragments or thin sections [1–6]. When compared to traditional dissolution of meteorite fragments, these methods preserve grains and textural information. However, these methods are exceptionally time consuming, cover very little sample surface area, and often result in locating few presolar grains.

X-ray computed tomography (CT) is a non-destructive imaging technique that generates a three-dimensional representation of a sample in terms of an X-ray attenuation image. X-ray CT is used extensively in many fields of research and in industry, though its application to locating and identifying graphite and SiC grains in meteorites and other precious samples from sample-return missions is limited. X-ray CT is promising for this task because of its potential to locate and identify 10s to 100s of presolar grains while preserving the sample. The X-ray CT images can also be used to efficiently target specific regions in the sample for more precise characterization by NanoSIMS or for subsequent analyses, such as by resonance ionization mass spectrometry (RIMS). In this work, we present ongoing work in the development of an X-ray CT based paradigm for imaging fragments of meteorite sample Jbilet Winselwan (hereafter referred to as Jbilet) to locate and identify presolar grain types. Ultimately, X-ray CT will be used to image Ryugu fragments to locate and identify presolar grains and place presolar grains in mineralogical context. The X-ray CT image of the full Ryugu fragment will be used to intelligently target smaller regions of interest for subsequent isotopic analyses by NanoSIMS and RIMS.

Methods: To develop X-ray CT imaging techniques, a ~150 μm diameter fragment of Jbilet was mounted on carbon tape on an SEM stub. This was imaged on a Zeiss Xradia 510 Versa using a conventional acquisition and subsequent tomographic reconstruction by cone-beam filtered back projection. The reconstructed image consists of a three-dimensional array of volumetric picture elements (voxels), each assigned a gray value corresponding to the attenuation of X-rays by the material(s) contained within the voxel. The ability to distinguish features in the sample is dependent on the ability to detect changes in the reconstructed gray values. X-ray attenuation is a function of material composition (namely, atomic number, and physical density) and photon energy. Conventional cabinet X-ray systems typically use vacuum tube X-ray sources, which generate polychromatic ‘bremsstrahlung’ X-rays, i.e., characterized by a broad range of photon energies. However, since conventional reconstruction algorithms assume monochromatic X-rays, changes in the reconstructed gray values are not linearly related to changes in atomic number and/or physical density. The absence of sensitivity to photon energy in conventional X-ray CT imaging means that it is difficult to distinguish features with similar material properties, such as presolar grains.

One of our long-term objectives is to perform multi-spectrum acquisitions for direct material characterization by leveraging so-called ‘dual-energy’ acquisitions: two datasets acquired under distinct X-ray spectra, and a home-grown algorithm for decomposing the acquired data into voxel-wise effective atomic number and electron density [7]. As a precursor to our long-term objective, in this study we performed a conventional ‘single-spectrum’ acquisition at 40 kV tube acceleration voltage with a voxel size of 240 nm (Fig. 1). The reconstructed image was subsequently analyzed with VGStudio (Volume Graphics GmbH) and its foam/powder analysis functionality to identify individual particles and to extract their morphological and gray value statistics.

Results: Despite the previous caveat on relating gray value changes to material differences, features with substantially different attenuation properties could be distinguished using the mean gray value of the voxels contained within the particle regions. Furthermore, we can compare the extracted particle morphology, such as sphericity, diameter, and volume, to expected morphology for each grain as an additional criterion for particle classification. Based on these criteria, we make the following observations: (1) pores are typically less than 15 μm in diameter; (2) larger spherical voids approximately 20 μm in

diameter are surrounded by purportedly concentric shells of high attenuation particles with a finer particle size compared to the matrix, and (3) particles with the highest mean attenuation values are highly spherical and generally less than 5 μm in diameter. Using the data collected in this study in concert with previous studies of Jbilet [8,9], we hypothesize the identification of various discrete particles. For instance, that the larger, spherical features could be chondrules or chondrules with alteration phases and smaller high mean grey value spherical particles could be metal blebs.

Future work: We have identified several ways to overcome identified limitations with X-ray CT, such as reducing imaging artifacts, improving image quality, and spatial and attenuation resolution. For instance, without energy sensitivity in the acquisition and subsequent reconstruction, it is difficult to separate grains with similar morphology but distinct material properties, like SiC and graphite. Beam-hardening artifacts (such as false high gray value regions due in large part to the absence of energy sensitivity observed at the exterior edge of the meteorite as shown in Fig. 2) can interfere with the correct identification of features. By imaging a thinner fragment, we can use lower energy photons, which will result in reduced beam hardening artifacts and increased sensitivity to small changes in material properties within the sample.

We will also investigate the inclusion of external material references, such as synthetic SiC and graphite, into the measurement volume to serve as gray value benchmarks for identifying the same materials inside the sample.

Acknowledgments: We thank G. Brenneka for the Jbilet Winselwan meteorite sample and A. Mohan for reconstruction assistance. This work was performed under the auspices of the U.S. Department of Energy by Lawrence Livermore National Laboratory under Contract DE-DEAC52-07NA27344 and was supported by the Laboratory Directed Research and Development Program at LLNL under project 20-ERD-030 and 23-LW-015. LLNL-ABS-854399.

References: [1] Nguyen A. N. et al. (2007) *ApJ*, 656, 1223–1249. [2] Keller L. et al. (2012) *MicroSC*, 18, 1704–1705. [3] Davidson J. et al. (2014) *GCA*, 139, 248–266. [4] Sanghani M. N. et al. (2021) *ApJS*, 352, 1–26. [5] Barosch J. et al. (2022) *ApJL*, 935, 1–12. [6] Nguyen A. N. et al. (2023) *Sci. Adv.*, 9, eadh1003. [7] Azevedo S. G. et al. (2016) *IEEE Trans Nucl Sci*, 63, 341–350. [8] Friend P. et al. (2018) *Meteorit. Planet. Sci.*, 53, 2470–2491. [9] King A. J. et al. *Meteorit. Planet. Sci.*, 54, 521–543.

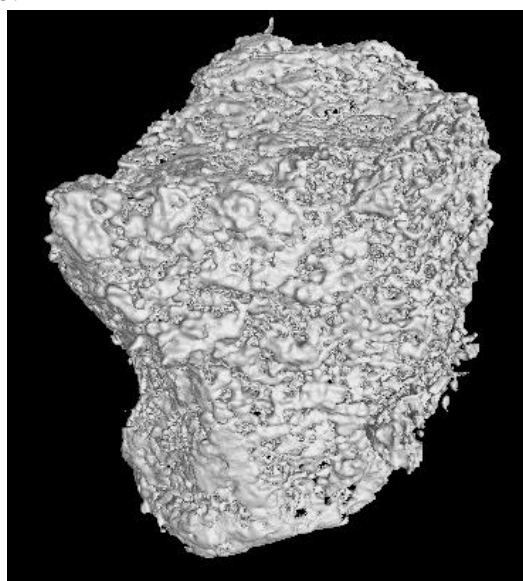


Figure 1. X-ray CT image of a $\sim 150\ \mu\text{m}$ diameter Jbilet fragment.

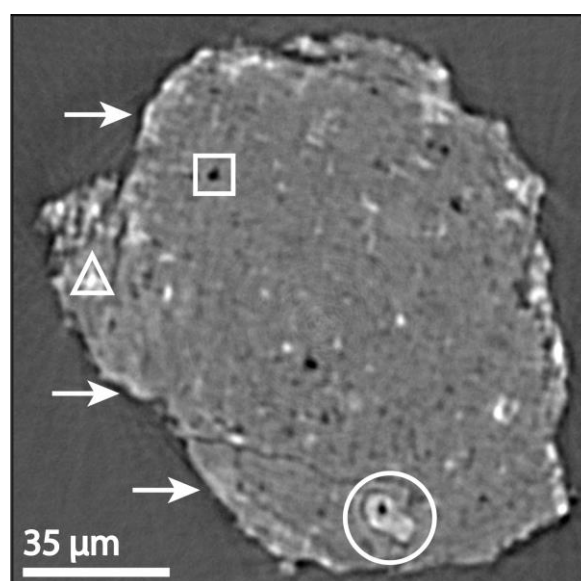


Figure 2. Cross section slice through a reconstructed X-ray CT image of Jbilet fragment. Examples of observed characteristics: square is a pore, triangle is metal bleb, and the circle is a chondrule. Arrows point to the “beam hardening” artifact that appears around the meteorite edge.

X-ray nano-CT and TEM-EDS Analyses of Impact Melt Splashes on Ryugu Samples

Megumi Matsumoto^{1*}, Junya Matsuno², Akira Tsuchiyama^{2,3}, Tomoki Nakamura¹, Yuma Enokido¹, Masahiro Yasutake⁴, Kentaro Uesugi⁴, Akihisa Takeuchi⁴, Satomi Enju⁵, Shota Okumura⁶, Itaru Mitsukawa⁶, Mingqi Sun³, Akira Miyake⁶, and the Hayabusa2 initial analysis team.

¹Department of Earth Sciences, Tohoku University, Tohoku University, Miyagi 980-8578, Japan. ²Research Organization of Science and Technology, Ritsumeikan University, Shiga 525-8577, Japan. ³Chinese Academy of Sciences (CAS) Key Laboratory of Mineralogy and Metallogeny/Guangdong Provincial Key Laboratory of Mineral Physics and Materials, Guangzhou Institute of Geochemistry, CAS, Guangzhou 510640, China. ⁴Japan Synchrotron Radiation Research Institute (JASRI), SPring-8, Hyogo 679-5148, Japan. ⁵Earth's Evolution and Environment Course, Department of Mathematics, Physics, and Earth Science, Ehime University, Ehime 790-8577, Japan. ⁶Division of Earth and Planetary Sciences, Kyoto University, Kyoto 606-8502, Japan.

Introduction: Ryugu samples are chemically and mineralogically similar to CI chondrites, and consist mainly of Mg-rich phyllosilicates, Fe-Ni-sulfides, magnetite, carbonates, hydroxyapatite, organic matters, and other minor minerals [1–5]. Some Ryugu particles experienced space weathering on the asteroid surface and exhibit amorphized and melted sample surfaces formed by solar wind irradiation and micrometeoroid bombardments [6]. A0067 and A0094 particles are among the space weathered Ryugu samples [6] and have flat sample surfaces which exhibit a lot of microcraters and impact melt splashes. In the present study, we investigated one relatively large microcrater (A0067-crater#1) and two impact melt splashes (A0067-melt#1 and A0094-melt#1) on the two particles (Fig. 1) by scanning electron microscope equipped with energy dispersive X-ray spectroscopy (SEM-EDS), X-ray nano-tomography (XnCT), and scanning transmission electron microscope (STEM) equipped with EDS to unveil the nature of the impactors hit on the asteroid Ryugu.

Results and Discussion: A0067-melt#1 shows round shape (~20 μm in diameter) and is composed of a Mg-Fe-rich glassy silicate main body and an Fe-rich opaque drop (~10 μm) attaching on the glassy silicate. It was extracted from the A0067 particle using focused ion beam technique and analyzed by XnCT and STEM-EDS. The analyses revealed that A0067-melt#1 is attached onto the saponite-rich coarse phyllosilicate layer (~1–4 μm in thickness) [2] developed along with the A0067 main body surface. Some gaps occur between the phyllosilicate sheets. These probably formed from shrinking of the phyllosilicate layers associated with volatile losses caused by the attaching of the hot impact melt splash. The glassy silicate in A0067-melt#1 has homogeneous Mg-Fe-rich composition with the ratio Mg/(Mg+Fe) in atom (hereafter Mg#) of ~0.64 and contains only small amounts of Fe-Ni metal-sulfide spherules (<100 nm). The Fe-rich opaque drop consists of dendritic crystals of α -(Fe-Ni) (~200–300 nm) embedded in the matrix composed mainly of troilite and minor pentlandite, and probably formed by a rapid cooling of an Fe-S-Ni melt.

A0094-melt#1 shows hourglass-like morphology (~15 \times 5 μm) and is probably made of two Mg-Fe-rich glassy silicate drops connected to each other. XnCT-STEM-EDS analyses revealed that A0094-melt#1 is compositionally inhomogeneous and shows patchy structure with Fe-rich (Mg# 0.52–0.55) and Fe-poor (Mg#~0.79) glassy silicate regions (2–5 μm in size). The boundaries between the regions are unclear. Spherical voids (a few tens of nanometers to ~2 μm) are abundant both in the Fe-rich and the Fe-poor regions. The Fe-poor region contains almost no crystalline phase whereas the Fe-rich region contains spherical and irregular-shaped Fe-Ni sulfides (<500 nm) and olivine grains (1–2 μm). Some aggregates (0.3–1 μm) consisting mainly of spongy inorganic carbon, irregular-shaped Fe-Ni sulfides, and Mg-rich silicates were also observed in A0094-melt#1. The aggregates are textually similar to primitive organic materials reported in anhydrous chondritic IDPs and carbonaceous chondrites [7], and might have formed from such primitive organic matters through volatile losses caused by impact induced heating.

A0067-crater#1 is ~5 μm in diameter. XnCT-STEM-EDS analysis revealed that A0067-crater#1 is ~4 μm in depth and traps small amount of mixture of glassy silicate

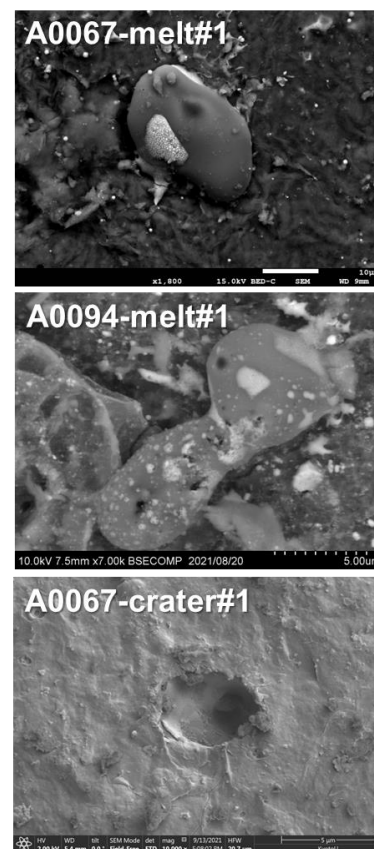


Fig. 1. FE-SEM images of A0067-melt#1, A0094-melt#1, and A0067-crater#1.

and troilite. The mixture should be an impact melt and shows flow structure consisting of glassy silicate and troilite layers (30–250 nm in thickness) stacking with each other. The glassy silicate layer is compositionally inhomogeneous and separated into Si-poor and Si-rich glasses. Both the silicate glasses contain spherical voids (<200 nm) and Fe-Ni sulfide spherules (<100 nm). The Si-poor glass (Mg#~0.72) is abundant compared to the Si-rich glass and compositionally similar to the glassy silicates in A0067-melt#1 and A0094-melt#1. The Si-rich glass selectively occurs along with the crater wall and probably formed *in-situ* from a Si-rich source material originally distributed on the A0067 particle surface. In the present study, we observed thin (<100 nm) Si-rich layers on A0067 and A0094 particle surfaces. These might correspond to the Si-rich vapor deposits previously reported on surfaces of some space weathered Ryugu particles [6] and may be the source of Si-rich glass in A0067-crater#1.

In the impact melts, different source materials such as impactors and Ryugu surface materials would have been mixed. The impact melts studied consist mainly of Mg-Fe-rich glassy silicate parts whose major element compositions (including Fe-Ni sulfide and olivine grains) are plotted along with an extension of a line connecting the CI (solar) composition [8] and the Fe-vertex in a (Si+Al)–Mg–Fe ternary diagram (Fig. 2). This suggests the impact melts studied have common source materials and the compositional trend seems to represent a mixing line of the source materials. A0094-melt#1 shows compositional inhomogeneity suggesting an incomplete mixing of the source materials, and the Fe-poor and the Fe-rich regions might be proximate to the original source materials. The Fe-poor region is compositionally similar to the Mg-rich phyllosilicate matrix in the Ryugu samples (Fig. 2) [2], which consists >80 vol.% of Ryugu samples, and probably sourced from Ryugu surface materials. On the other hand, the Fe-rich region has CI-like composition which deviate from the compositions of Ryugu’s phyllosilicates and other Ryugu components (Fig. 2). This suggests that Ryugu is not the source of the Fe-rich region and that the Fe-rich region was probably sourced from the impactors. The known small planetary materials having CI-like compositions are interplanetary dust particles (IDPs) and micrometeorites derived from asteroids and comets. Among those, anhydrous chondritic IDPs have bulk compositions which match well with the compositional range of the impact melts studied (Fig. 2) [9], and might be the source of the Fe-rich region. This is consistent with the presence of the carbonaceous aggregates, which might have formed from primitive organic matters, in A0094-melt#1. These mean that the impact melts studied might have formed by anhydrous chondritic-IDPs impacts on the Ryugu’s surface. Further study of many more impact melt splashes and microcraters will give important information about the variation and flux of the impactors that hit on asteroid Ryugu.

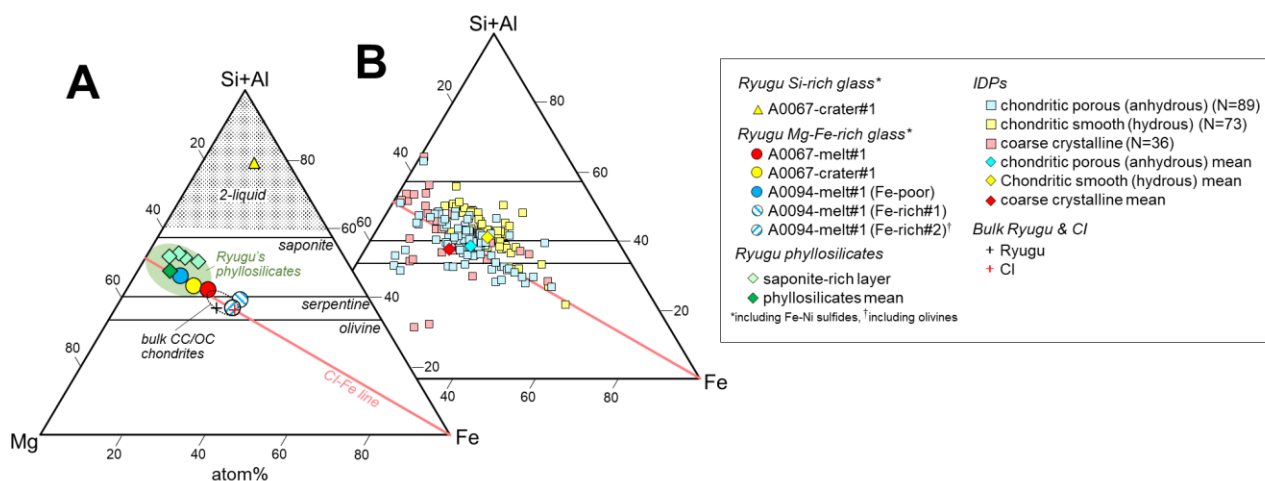


Fig. 2. (Si+Al)–Mg–Fe atom% ternary diagram of compositions of the melt splashes. (A) The major element compositions of the melt splashes studied and (B) those of IDPs. The compositions of IDPs are from [9], Ryugu’s bulk composition is from [1], and the composition of the phyllosilicates in the Ryugu samples is from [2]. The compositional field of Ryugu phyllosilicates (774 analyses) [2] is shown as a green colored oval.

Reference: [1] Yokoyama et al. (2023) *Science*, **379**, eabn7850. [2] Nakamura et al. (2023) *Science*, **379**, eabn8671. [3] Ito et al. (2022), *Nat. Astron.* **6**, 1163–1171. [4] Nakamura et al. (2022) *Proc. Jpn. Acad. Ser. B* 98:227. [5] Yamaguchi et al. (2023), *Nat. Astron.* **7**, 398–405. [6] Noguchi et al. (2023) *Nat. Astron.* **7**, 170–181. [7] Matrajt et al. (2012) *Meteorit. Planet. Sci.* **47**, 525–549. [8] Lodders (2021) *Space Sci. Rev.* **217**, 44. [9] Schramm et al. (1989) *Meteoritics* **24**, 99–112.

Comparison of Thermal Diffusivity between Ryugu grains and Carbonaceous Chondrites

Takuya Ishizaki¹, Ryota Fukai¹, Rei Kanemaru¹, Keisuke Onodera², Yoshinao Yasuda³,
Toru Yada¹, Masanao Abe¹, Tatsuaki Okada¹, Tomohiro Usui¹

¹Japan Aerospace Exploration Agency, 3-1-1 Yoshinodai, Sagamihara, Kanagawa 252-5210, Japan

²The University of Tokyo, 7-3-1 Hongo, Bunkyo-ku, Tokyo 113-0033, Japan

³Kwansei Gakuin University, 1-155 Uegahara Ichiban-cho, Nishinomiya, Hyogo 662-8501, Japan

Introduction: According to the general planetary formation scenario, the Solar System bodies evolved over a long period of time through repeated collision, fragmentation, and aggregation of planetesimals formed in the solar nebula. Thermal evolution, which induces various physicochemical reactions such as aqueous alteration, thermal metamorphism, and volcanism, is important for the evolution of planets. The temperature history inside the planetesimals followed in thermal evolution can vary greatly depending on when and how large they agglomerate and their effective thermal conductivity. Therefore, it is essential for the theory of planetary system formation to know the thermal conductivity of asteroids and meteorites, especially those that are thought to have existed since the early stages of planetary system formation.

The Ryugu sample brought back in 2020 by Hayabusa2 was found to be a primitive Ivuna-type carbonaceous chondrite, which is close to the average chemical composition of the Solar System [1]. Additionally, the elastic properties of the Ryugu grains were found to be similar to those of the Tagish Lake meteorite [2]. On the other hand, the thermophysical properties of Ryugu grains were found to vary widely from grain to grain [3]. Although this is the most important parameter in understanding the thermal history of asteroidal parent bodies, the cause of this variation has not been clarified. In this study, we measured the thermal diffusivities of Ryugu particles and carbonaceous chondrites using the lock-in thermography (LIT) periodic heating method [3], which was also used for the initial analysis of Ryugu grains to evaluate how the thermal properties of Ryugu grains are related to those of other carbonaceous chondrites.

Samples and Methodology: In this study, the thermal diffusivities of Ryugu and the carbonaceous chondrites were measured. A breakdown of the samples is as follows: three grains of Ryugu (A0172, A0038, and C0054), three grains of Ivuna (CI), one grain of Murchison (CM2), one grain of Tarda (C2-ungrouped), three grains of Tagish Lake (C2-ungrouped), and two grains of Allende (CV3). Bulk densities of the sample were also measured by obtaining weights and volumes of the sample. The volume was obtained by using an X-ray computed tomography (X-CT) device (SKYSCAN 1272). The X-CT images were also utilized to avoid cracks inside the sample, because the cracks may specifically affect to the results of the thermal diffusivity measurements.

In the measurement by the LIT periodic heating method, a spot on the sample is periodically heated using a laser, and the temperature response is measured by LIT to obtain the phase lag distribution on the sample surface. Then, the thermal diffusivity is analyzed from the gradient of the phase lag according to this equation; $D = \pi f / (d\theta/dr)^2$. Here, D is thermal diffusivity, f is heating frequency, θ is phase lag and r is distance from heating point. A measurement apparatus was originally constructed by combining a LIT (InfraTec ImageIR® 8350hp) with InSb cooled detector and 3x objective lens which provides a spatial resolution of 5 μm , optics, and a diode laser (633 nm, less than 10 μm of focus diameter). The laser beam was modulated according to the synchronized periodic signal from LIT, and an average power was estimated to be less than 10 mW. The schematic of the measurement is shown in Figure 1.

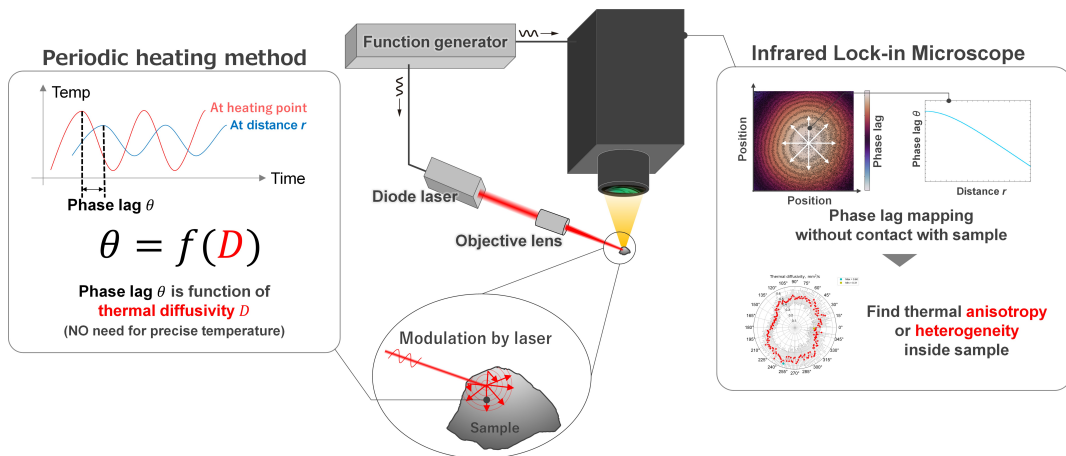


Figure 1 Schematic of the measurement.

The heating frequency was selected according to the sample size to avoid the influence of reflected temperature waves at the sample edge, and then measurements were performed at 20 Hz. The samples were measured under vacuum conditions of a pressure less than 10^{-4} Pa to refrain the effect of the surrounding air because the air causes the overestimate of the thermal diffusivity in the case of the low thermal diffusivity material.

Results and Discussion: The average value of the measured directional distribution of the thermal diffusivities of the Ryugu grains were $(1.5\text{--}3.7) \times 10^{-7} \text{ m}^2/\text{s}$. The thermal diffusivity of A0308 was particularly low, averaging $1.5 \times 10^{-7} \text{ m}^2/\text{s}$, which is the lowest value among all the Ryugu grains ever measured. The thermal diffusivities of the ten grains of carbonaceous chondrites were $(1.5\text{--}5.1) \times 10^{-7} \text{ m}^2/\text{s}$, with the Allende meteorite having a definitely higher value and the Tagish Lake meteorite having a definitely lower value than that of the others. The results for the other meteorites coincided within the margin of error.

Figure 2 shows the relationship of the thermal diffusivity and bulk density for each sample. Figure 1 also includes the results of the initial analysis of Ryugu [3], and reference values of Allende (CV3) measured by Soini et al. [4], and Murchison (CM2), Murray (CM2), Cold Bokkeveld (CM2), Jbilet Winselwan (CM2) and NWA 7309 (CM2) by Opeil et al. [5] are also shown as square plots. The results show a positive correlation between thermal diffusivity and bulk density, which is in agreement with reference values, except for Jbilet Winselwan and NWA 7309. Tagish Lake and Ryugu have the smallest thermal diffusivity and density among the groups that experienced the aqueous alteration, including Ryugu. On the other hand, the density and thermal diffusivity of Allende are confidentially larger than the other carbonaceous chondrites and Ryugu. There are several possible causes explaining the variation: (i) thermal diffusivities and densities of Ca- and Al-rich inclusions and chondrules are possibly larger than those of the matrix and Allende has a larger volume fraction of them [6]; (ii) the thermal diffusivity of the matrix possibly to be larger when olivine content is higher; (iii) the thermal diffusivity may be reduced by pores and cracks in the matrix developed during an aqueous alteration. We still have no clear conclusion for the cause of variation. Nevertheless, the variation of the thermal diffusivity and relationship with the density is critical for the thermal evolution of the planetesimals.

Also, Ryugu grains show a thermal diffusivity-bulk density relationship more similar to the Tagish Lake than to the Ivuna sample, which has a similar elemental composition to Ryugu. This result is in agreement with the elastic properties measured by Onodera et al. [2] and suggests that in carbonaceous chondrites with petrological classifications 1 or 2, thermo-mechanical properties may be dominated by mechanical and structural features consisting of the matrix, inclusions, and voids inside the grain. The grain of the lowest thermal diffusivity in Ryugu samples do not have a smaller bulk density than that of other Ryugu grains. Furthermore, the results of the thermal diffusivity distribution analysis indicate that the decrease

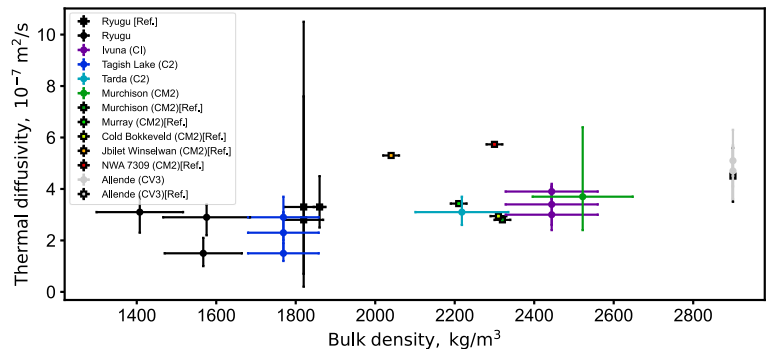


Figure 2 Thermal diffusivity vs. bulk density of Ryugu and carbonaceous chondrites.

in thermal diffusivity is unlikely due to cracking because the angular distribution of the thermal diffusivity seemed almost isotropic. In other words, this suggests the possibility that there is a heterogeneous distribution of the pore structure or tiny inclusions that reduce the thermal diffusivity while maintaining the bulk density.

To investigate the relationship between elastic wave velocity and thermal diffusivity, we additionally measured the primary elastic wave (P-wave) velocities of some samples as follows: one grain of Ivuna (CI), one grain of Murchison (CM2), one grain of Tarda (C2-ungrouped), and three grains of Tagish Lake (C2-ungrouped). The pulse transmission method was used for the measurements. Details of the measurements of the P-wave velocity are described in a previous report [7]. The result is shown in Figure 3, and the reference value of Ryugu is from Ref. [3, 5]. Figure 3 shows that there is a positive correlation between thermal diffusivity at the range of 0–2 km/s for the P-wave velocities. However, for P-wave velocities above 2.0 km/s, the thermal diffusivity tends to approach a constant value for P-wave velocity. Although the number of measurements is insufficient to clearly understand the cause of this trend, since the thermal diffusivity is more susceptible for the structural factors than the elastic wave velocity, it is possible that the structural factors in the grain may differ around the P-wave velocity of 2.0 km/s (e.g., whether the cracks are in a contact or non-contact at interface). The relationship between thermal diffusivity and elastic wave velocity will be able to provide an effective basis for understanding the internal structure of Ryugu and chondrite grains, by increasing sampling numbers for the carbonaceous chondrites in petrological classifications 1 or 2 and 3.

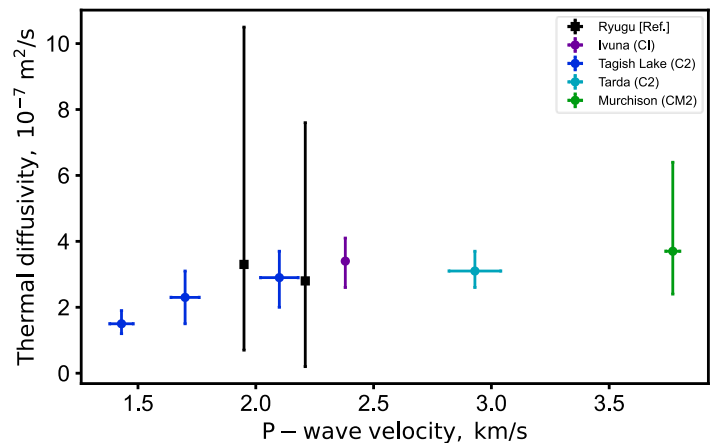


Figure 3 Thermal diffusivity vs. P-wave velocity of Ryugu and carbonaceous chondrites.

References

- [1] T. Yokoyama et al., *Science*, abn7850 (2022).
- [2] K. Onodera et al., *ESS Open Archive*, May 25 (2023).
- [3] T. Ishizaki et al., *Int. J. Thermophys.*, 44(4), 51, 2023.
- [4] Soini et al., *Meteorit. Planet. Sci.* 55, 402–425 (2020).
- [5] Opeil et al., *Icarus*, 208(1), 449–454, (2020).
- [6] H. Y. McSween, Jr. and G. R. Huss, “*Cosmochemistry*,” Cambridge Univ. Press, 169 (2010).
- [7] Onodera et al., *Proc. Jpn. Soc. Planet. Sci. Fall Mtg. 2023* (2023).

Spatial relationship between macromolecular organic matter and organic-bearing phyllosilicates in Ryugu grain.

Toru Matsumoto¹, Takaaki Noguchi², Tohru Araki³, Takuji Ohigashi⁴, Yohei Igami², and Akira Miyake²

¹The Hakubi center for Advanced Research, Kyoto University, ²Division of Earth and Planetary Sciences, Kyoto University, ³Institute for Molecular Science, ⁴High Energy Accelerator Research Organization.

Introduction: Regolith samples recovered from the C-type asteroid Ryugu show chemical and petrological characteristics similar to those of CI carbonaceous chondrites [e.g., 1-3]. They consist of primitive components of the early solar system, including water and organic matter, but are highly modified in the parent body by aqueous alteration. Insoluble organic macromolecules (IOM) in Ryugu grains are the dominant components of organic matter in Ryugu's materials [3]. The chemical structures, distributions, and morphologies of the macromolecular organic matter can be tracers of the evolution of organic materials in the interstellar medium, the protosolar disk, and the aqueous environment in the parent body of Ryugu [3]. Recent analysis of the interlayer spaces of phyllosilicate minerals in Ryugu grains suggested the presence of organic molecules in clay structures [4, 5]. The infrared absorption band at around 3 μm obtained from Ryugu grains may come from N-H bearing molecules trapped in the interlayers of phyllosilicates [6]. These results suggest that phyllosilicates have been affected by organic matter during the aqueous alteration. Detailed investigation of the interlayer spaces of phyllosilicates and their spatial association with macromolecular organic matter will provide insight into the interaction between minerals, water, and organic matter in the parent body of Ryugu. In this study, we focused on carbon-rich regions in a Ryugu grain and examined the spatial relationship between organic materials and phyllosilicates, together with their chemical features.

Methods: A Ryugu grain from the chamber A (grain No. A0142) was distributed by JAXA as a sample for the international announcement of opportunity and was used in this study. The surface features of the grain was observed using a field-emission (FE)-scanning electron microscope (SEM) (JSM-7001F). Electron-transparent sections were extracted from the regions of interest using a focused ion beam system (FIB Helios NanoLab G3 CX). Scanning transmission X-ray microscopy (STXM) imaging was performed to obtain X-ray absorption near edge structure (XANES) spectra from the sections. The bonding structure of carbon was investigated using XANES spectra at the carbon K-edge (at 280 eV-320 eV). After STXM analysis, the sections were observed using field-emission transmission electron microscope (TEM) (JEOL JEM2100F).

Results: Backscattered electron images of the grain surface show the concentration of organic matter embedded in the phyllosilicate matrix (Fig. 1a). Several carbon-rich spots were found on the grain surface. We investigated the largest carbon-rich region with approximately $17 \times 8 \times 9 \mu\text{m}$ in size (Fig. 1ab). Carbon-XANES spectra of the carbon-rich region include major peaks of aromatic carbon (285 eV) and carboxyl carbon (288.5 eV), and those of phyllosilicate matrix in the vicinity of the carbon-rich region show peaks of aromatic carbon (285 eV), carboxyl carbon (288.5 eV), aliphatic carbon (287.5 eV), and carbonates (290.4 eV). TEM analysis showed that organic materials and fibrous phyllosilicates are finely intermixed in the carbon-rich region. Hereafter, we call the carbon-rich region as the carbon-phyllosilicate aggregate (CPA). Distinct morphologies of organic materials, such as the organic globules, were not identified in the CPA. The surrounding matrix consists mainly of fibrous phyllosilicates, magnetite, iron sulfides, and carbonates. High-resolution TEM images showing layered structures of the fibrous phyllosilicates (Fig. 1c) enabled us to investigate the interlayer distance of the phyllosilicates. The majority of the fibrous phyllosilicates in the CPA and the matrix have interlayer distances of 0.7~0.75nm, and 1.0-1.2nm. These values correspond to typical interlayer distances of serpentine and saponite in Ryugu samples, respectively [2]. On the other hand, fibrous phyllosilicates with interlayer distances of 1.23-1.35 nm were occasionally observed in the CPA and in the matrix close to the carbon-rich region (Fig. 1c).

Discussion: The enrichment of aromatic and carboxylic carbon in the XANES spectra from the CPA is similar to the spectral features of highly-aromatic or aromatic macromolecular carbon in Ryugu samples [3]. The concentration of aromatic organic matter may have occurred by redistribution and/or synthesis of organic matter during fluid activity in the parent body. It is also possible that large chunks of organic matter have been incorporated during the initial accretion of the parent body, in the form of primitive materials originated from the outer solar system [7]. The appearance of aliphatic carbon in the matrix is consistent with the previous XANES study of Ryugu samples, in which aliphatic organics were detected in association with phyllosilicates [8]. Previous X-ray diffraction measurements of Ryugu samples detected 001 reflection of smectite at 1.26 nm [4]. The relatively large interlayer distance was interpreted as the expansion of the interlayer space due to the presence of organic molecules [4]. Accordingly, the interlayer distances of 1.25-1.35 nm found in our sample suggest that organic species

are intercalated into the phyllosilicates. The spatial relationship between the CPA and the possibly organic-bearing phyllosilicates suggests that macromolecular organic matter could have interacted with surrounding phyllosilicates during aqueous alteration, as suggested by analyses of carbonaceous chondrites [9, 10].

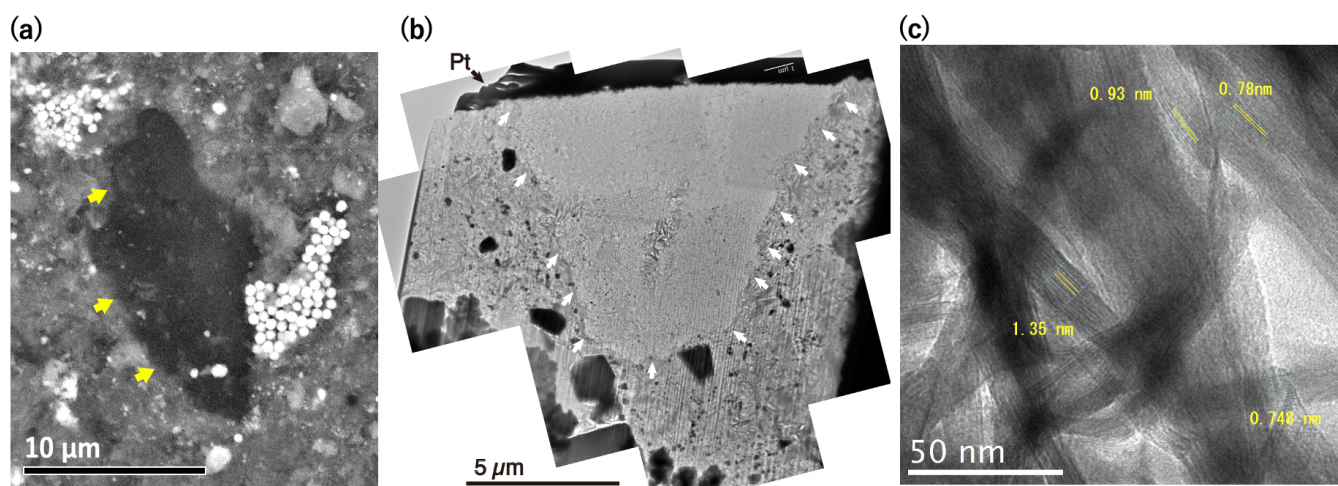


Figure 1. SEM and TEM analysis of the carbon-rich region of Ryugu grain (A0142). Backscattered electron image (a) and bright-field TEM image (b) of the carbon-phyllsilicate aggregate (CPA). Arrows indicate the interface between the CPA and surrounding phyllosilicate matrix. (c) High-resolution TEM image of fibrous phyllosilicates near the CPA. Interlayer distances are shown in the figure.

References: [1] Yokoyama et al. 2022. *Science* 379.6634, eabn7850. [2] Nakamura et al. 2022. *Science* 379.6634, eabn8671. [3] Yabuta et al. 2023. *Science* 379. 6634, eabn9057. [4] Viennet et al. 2023. *Geochem. Persp. Let.* 25, 8-12. [5] Damien et al. 2023. *Meteoritics & Planetary Science* under review. [6] Pilorget et al. 2022. *Nat. Astron.* 6, 221-225. [7] Duprat et al. 2010. *Science* 328, 742-745. [8] Ito et al. 2020. *Nature Astron.* 6:1163-1171. [9] Garvie and Buseck, 2007. *Meteoritics & Planetary Science* 42, 2111-2117. [10] Guillou et al. 2014. *Geochim. Cosmochim. Acta*, 131, 368-392.

Analysis of a thermal correction method for the MIRS infrared spectrometer: preparation for the future observations of the Martian moons Phobos and Deimos

G. David¹, M. Delbo², A. M. Barucci¹, F. Merlin¹, P. Beck³, S. Fornasier¹ and G. Poggiali¹

¹ *LESIA, Observatoire de Paris, Université Paris Cité, Université PSL, Sorbonne Université, CNRS, Meudon, France*

² *Laboratoire Lagrange, Observatoire de la Côte d'Azur, Université Côte d'Azur, CNRS, Nice, France*

³ *Institut de Planétologie et d'Astrophysique de Grenoble, OSUG/CNRS, 122 rue de la piscine, F-38000 Grenoble, France*

Introduction: The Martian Moon eXploration (MMX) mission is scheduled to be launched to the Martian system in 2024 [1]. The scientific payload will include the MMX InfraRed Spectrometer (MIRS, [2]), an instrument dedicated to the study of Mars and its satellites: Phobos and Deimos. MIRS data will contribute, together with the other instruments and the sample return analysis, to understand the origin of the two Martian moons. It will help to decipher whether they are captured asteroids or rather formed by accretion from a debris disk, the latter resulting from a giant impact between Mars and a planetesimal. In the spectral range covered by MIRS (0.9-3.6 μm), several components of geological interest will be studied through their spectral properties such as anhydrous and hydrous silicate minerals, water ice, or organic matter. Constraining the presence and relative abundance of these phases will help to determine the Martian moons' formation processes. However, several absorption bands associated with these compounds are in the spectral region beyond $\sim 2.5 \mu\text{m}$, where the signal collected by the instrument is a combination of reflected sunlight and thermal emission from the observed surfaces. The thermal emission - the so-called thermal tail - can strongly modify the continuum of the spectra and the width of the absorption bands. Consequently, before proceeding to the mineralogical analysis and interpretation of future MIRS data, a thermal emission correction is needed. In this study, a simple method of thermal emission correction is tested on synthetic data to evaluate its potential and limitations.

Method: The thermal tails of spectra are mainly controlled by the surface's temperatures, roughness and emissivity. For airless bodies, such as Phobos and Deimos, the surface conditions can be highly fluctuating, between $\sim 130 \text{ K}$ and $\sim 300 \text{ K}$ [3]. Temperature and emissivity are often not well-constrained on planetary surfaces, but they can be estimated directly from the infrared spectra. In this work, we deliberately explored a simple empirical method of thermal tail removal, based on Planck blackbody fit, owing to the MIRS instrument will provide a large amount of data and a method running quickly will save computing time and make it easier data interpretation during MMX flight operations. We used the approach from [4], which was originally developed to correct the Moon Mineralogy Mapper (M^3) observations onboard the Chandrayaan-1 spacecraft. This approach is iterative and uses the assumption that the continuum of the reflected solar component is approximately linear beyond $2.5 \mu\text{m}$. The signal at short wavelengths (with no thermal contribution) is used to extrapolate the reflected component in the thermal tail part of the spectra at a given wavelength. The differences between the projected reflectance and the original spectra, corresponding to the thermal contribution, are then fitted with a blackbody Planck function radiation, and a temperature can be derived. Emissivity (ϵ) is determined by using the projected I/F (the signal collected by the instrument normalized to the solar flux) at a specific wavelength and Kirchhoff's law ($\epsilon=1-I/F$). Here, we perform two iterations to adjust the temperature, using in the second run the previous corrected spectra. While in the first iteration, emissivity is considered as constant with wavelength, the second iteration will consider a wavelength-dependent emissivity (i.e., the Kirchhoff's law is used for each wavelength).

Synthetic data: Different spectral datasets were generated for the purpose of this study by means of a thermophysical model [5], which calculates thermal infrared spectra of airless bodies or sub-portions thereof as a function of several physical parameters such as albedo, roughness, thermal inertia, rotation period, direction of the rotation axis, as well as illumination and viewing geometry. The first dataset corresponds to seven synthetic reflectance spectra thought to be reasonably analogous to Phobos, for which thermal contribution at different temperatures from 262 K to 329 K has been added. In this first set of simulations, the scene corresponds to a flat facet of the Phobos shape model in nadir view. The second dataset includes the same parameters but this time, roughness has been generated by adding hemispherical section craters into the facet. This makes such that sub-facets with different inclinations with respect to the sun and the instrument compose the field of view. Each sub-facet contributes to the thermal infrared flux with its own temperature, which depends on the geometry relative to the sun. Finally, the last dataset is similar to the previous one but includes a fictitious absorption band centered at $3.2 \mu\text{m}$, to study its effect on thermal correction. In all our simulations, ϵ has been set to 0.9, which is thought to be consistent with the Martian moon surfaces.

Results: The first dataset is used to test the consistency between the temperature retrieved by the thermal correction model and the temperature used as input by the thermophysical model. Our results show that the first iteration gives an average of $\sim 0.8 \text{ K}$ of difference from the true temperature, while the second iteration increases the error on temperature retrieval with an average of $\sim 1.4 \text{ K}$ of difference. These results are consistent with the experiment made by [4], who found that the derived temperature by this approach of heated basalt in the laboratory was around 1 degree of the true measured temperature. The emissivity predicted by the model is also very consistent with the one used in the thermophysical model ($\epsilon=0.9$) to generate the

data. The first iteration predicts $\varepsilon \sim 0.88$ for all temperatures, whereas the second iteration predicts emissivity within 0.86-0.88. To determine the efficiency of the thermal correction, we calculated the mean absolute percentage error (MAPE), which quantifies the difference between each corrected spectrum and its spectrum of reference (i.e. spectrum generated without thermal contribution) that can be expressed as $MAPE = \sum_{\lambda > 2.5 \mu m}^n \left| \frac{y_{\lambda} - x_{\lambda}}{y_{\lambda}} \right| \frac{100}{n}$, where y_{λ} and x_{λ} are the I/F values of the reference and corrected spectra for each wavelength in the thermal part (i.e., $\lambda > 2.5 \mu m$). For the first data set, we found that corrected spectra have respectively MAPE scores of $\sim 1.25\%$ ($\sigma = 0.5\%$) and $\sim 0.21\%$ ($\sigma = 0.2\%$) on average for the first and second iterations, which is pretty good. For the second dataset, including roughness in the simulated scene, the complexity of the data slightly degrades the thermal correction (Figure 1, left panel). For all spectra, a small rise in reflectance can be observed after the thermal correction at the edge of the spectra due to an under-correction. Nevertheless, this residual thermal contribution is quite negligible as expressed by the good MAPE scores. On average, they are respectively equivalent to $\sim 3.1\%$ ($\sigma = 1.1\%$) and $\sim 1\%$ ($\sigma = 0.49\%$), for the first and second iterations, which is satisfying. Emissivity predicted by the model ($\varepsilon_{\text{iteration 1}} \sim 0.88$, $\varepsilon_{\text{iteration 2}} = 0.86-0.88$) is still very consistent with the reference and is similar to the emissivity guessed for the first dataset.

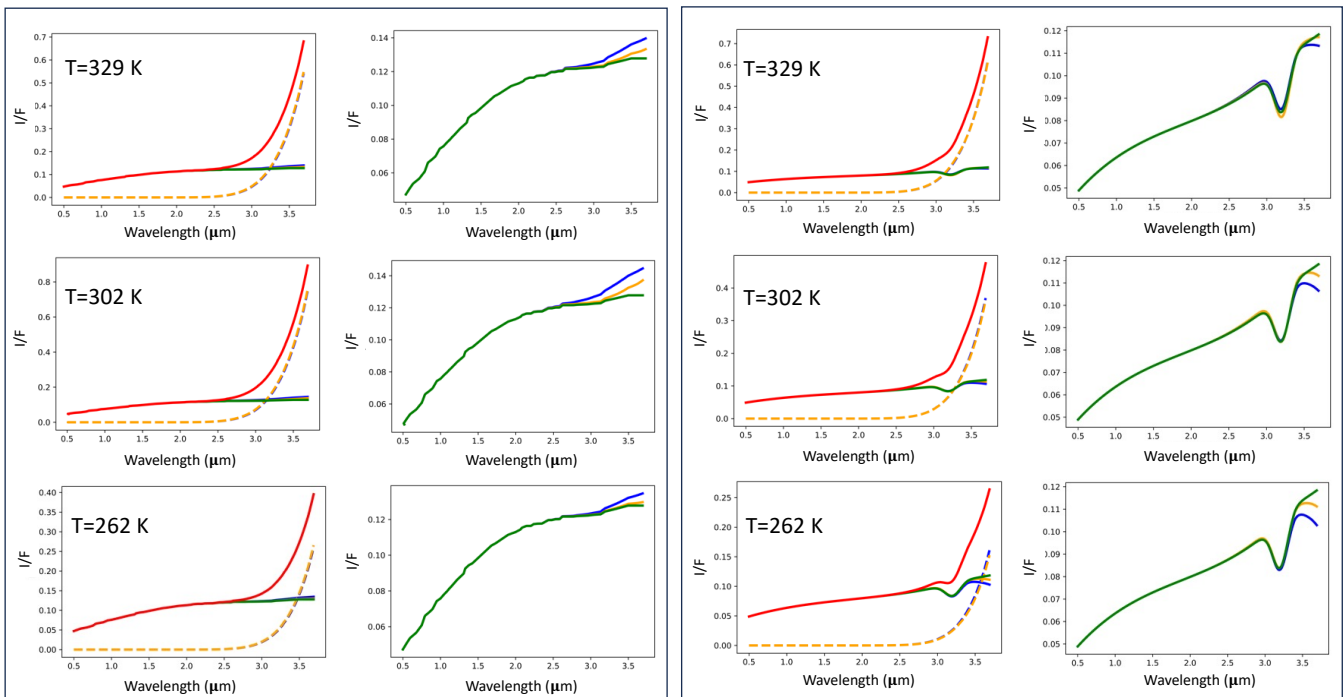


Figure 1. Results of thermal correction of several synthetic reflectance spectra of Phobos generated by means of a thermophysical model [5]. Spectra with thermal emission (red lines) are compared to the two iterations of thermal removal (first and second iterations are represented respectively in blue and orange). Green spectra correspond to the synthetic spectra simulated without the thermal contribution and they serve as a benchmark. Dash lines correspond to the Planck functions of the first and second iterations (respectively in blue and orange). The left panel shows the results for the second set of synthetic data, whereas the right panel corresponds to the third dataset with absorption bands.

For the synthetic spectra containing a synthetic absorption band at $3.2 \mu m$, the model of thermal correction seems to be still efficient (Figure 1, right panel). The MAPE scores of these spectra remain quite good with an average of $\sim 1.6\%$ ($\sigma = 0.61\%$) and $\sim 0.8\%$ ($\sigma = 0.01\%$). Emissivity is still overall in line with the one used to generate the data ($\varepsilon_{\text{iteration 1}} \sim 0.92$, $\varepsilon_{\text{iteration 2}} = 0.89-0.92$). Despite the relatively good MAPE scores, a drop in reflectance can be observed at the edge of the spectra (beyond $3.45 \mu m$), which was also observed in the work made by [4]. In terms of band depths, the differences with the references are in averages respectively equivalent to $\sim 7.3\%$ ($\sigma = 0.96\%$) and $\sim 4.7\%$ ($\sigma = 4.2\%$) for spectra corrected with one and two iterations.

Conclusion: In this study, we tested on simulated data of Phobos, the thermal correction method developed by [4]. Our results show that this method appears to be usable for the thermal correction of future MIRS observations. The correction seems to be efficient, especially for high surface temperatures. Moreover, by improving each time the MAPE scores with the second run of the data treatment, we confirmed the efficiency of the iterative approach. We also quantified the impact of the thermal correction on the absorption bands and found an overestimate of the band depths limited to a few percent. This is an ongoing work to improve the thermal tail removal in preparation for the planned activity of MIRS during the orbital phase of MMX mission.

References: [1] Kuramoto, K., et al., (2021), Earth Planets Space. 74(1), 1-31. [2] Barucci, M. A., et al., (2021), Earth, Planets, and Space. 73-211. [3] Giuranna, M., et al. (2011), Planetary and Space Science. 59(13), 1308-1325. [4] Clark, R. N., et al., (2011), Journal of Geophysical Research: Planets, 116(E6). [5] Delbo, M., et al., (2015), Asteroids IV, 1, 107-128.

A Comparative Carbon-XANES and -EELS study of Organic Material from Asteroid 162173 Ryugu and Ivuna.

H. G. Changela^{1,2}, L. Petera^{1,3}, J. C. Bridges⁴, Y. Kebukawa⁵, L. Hicks⁶, N. Topping⁴, C. S. Allen⁷, E. Chatzitheodoridis⁸, M. Ferus¹

1 Department of Spectroscopy, J. Heyrovsky Institute of Physical Chemistry, Czech Academy of Sciences, Czechia. 2 Department of Earth & Planetary Science, University of New Mexico, New Mexico, USA. 3 Department of Inorganic Chemistry, Charles University in Prague, Czechia. 4 Space Research Centre, School of Physics and Astronomy, University of Leicester, UK. 5 Department of Earth & Planetary Sciences, Tokyo Institute of Technology, Japan. 6 School of Geology, Geography, and the Environment, University of Leicester, UK. 7 electron Physical Science Imagine Centre, Diamond Light Source, Oxford, UK. 8 School of Mining, National Technical University of Athens, Greece. Email: changela@unm.edu

Introduction The arrival of samples from carbonaceous asteroids 16273Ryugu [1] 101955Bennu [2] provide a window into early Solar System organic evolution on a known asteroid. Organic material (OM) from carbonaceous asteroids is currently most accurately characterised *in situ* by coordinating synchrotron based scanning transmission X-ray microscopy (STXM) with transmission electron microscopy (TEM) on samples. Organic functional chemical variations can be measured by Carbon K-edge X-ray absorption near edge structure (XANES), whilst organic morphology and its mineral setting is characterised by subsequent TEM. Carbon-energy electron loss spectroscopy (EELS) offers the same possibility as C-XANES but with the advantage of being performed in a stand-alone TEM. Here we compare C-EELS with -XANES on OM from Asteroid Ryugu and the Ivuna CI chondrite prepared by dual beam focused ion beam (FIB)- scanning electron microscopy (SEM) and ultra microtome to assess the effects of electron beam dosage by all techniques.

Methods Two adjacent ~100 nm thick lamella were prepared using FIB-SEM (Fig. 1). Lamella 1 was prepared using Xe-plasma FIB-SEM with the Helios 5 Hydra DualBeam (CEITEC, Masaryk University (MUNI), Czechia) and analysed by TEM-C-EELS with the JEOL ARM200CF (ePSIC, Diamond Light Source, UK), followed by STXM-XANES at Beamline BL19A of the KEK Photon Factory, Japan. Lamella 2 (Fig. 1) was prepared by Xe-plasma FIB-SEM with the TESCAN AMBER X (TESCAN ORSAY holding a.s., Brno, Czechia) followed by STXM-XANES (i.e. no TEM) at the photon factory. Microtome samples of Ivuna were prepared using methods in [3] at CEITEC-MUNI with a Leica UC7. Organic material in a lamella from Ryugu grain C0105-03500000 provided by the Hayabusa-2 preliminary examination SAND team prepared using the University of Leicester's FEI Quanta 3D was also measured by C-EELS at ePSIC.

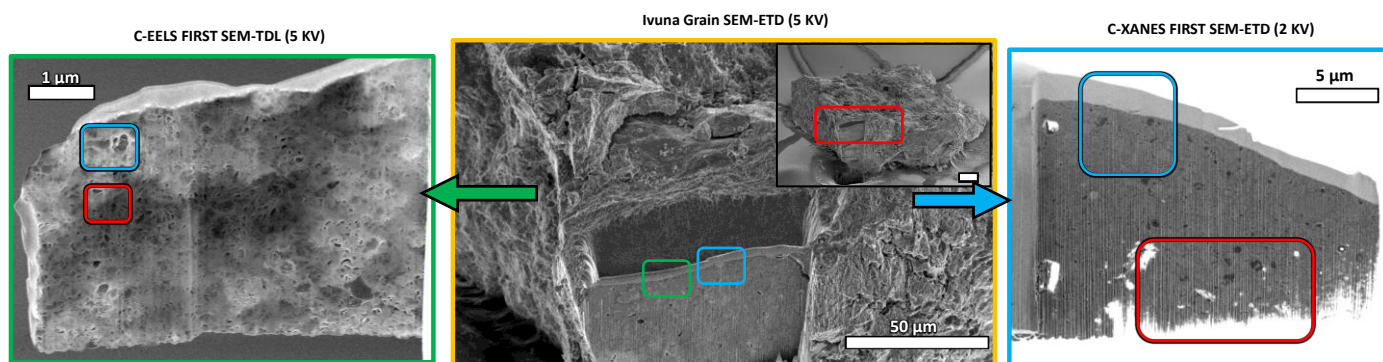


Figure 1. SE image of a grain of Ivuna on carbonate sticky and coated with 5 nm Au. Large cross section at the front of the grain was the location where 2 adjacent FIB lamella were extracted: one with C-K edge EELS then XANES (left extraction) and the other direct XANES (right lamella). Blue and red rectangle mark the ROIs where the EELS and XANES maps were taken (Fig. 2).

Results Electron beam exposure to chondritic OM during SEM, TEM and EELS changes its functional chemistry, in both its macromolecular and particularly in soluble/insoluble form within phyllosilicate (Fig. 2). A peak at ~290.4 eV attributed to carbonate -O-C=O-O- bonds is observed under 200 KV electron doses by TEM, STEM imaging and by EELS spectral mapping. This feature is absent from microtome samples measured by XANES. A bulge in the EELS spectra consistent with amorphous an carbon σ^* peak (~288 – 315 eV) is found in organic particles. The carboxylic (288.5 eV) peak found in diffuse OM within phyllosilicates (e.g. Graph 2) is replaced by the carbonate one at 290.4 eV (Graphs 1 & 4).

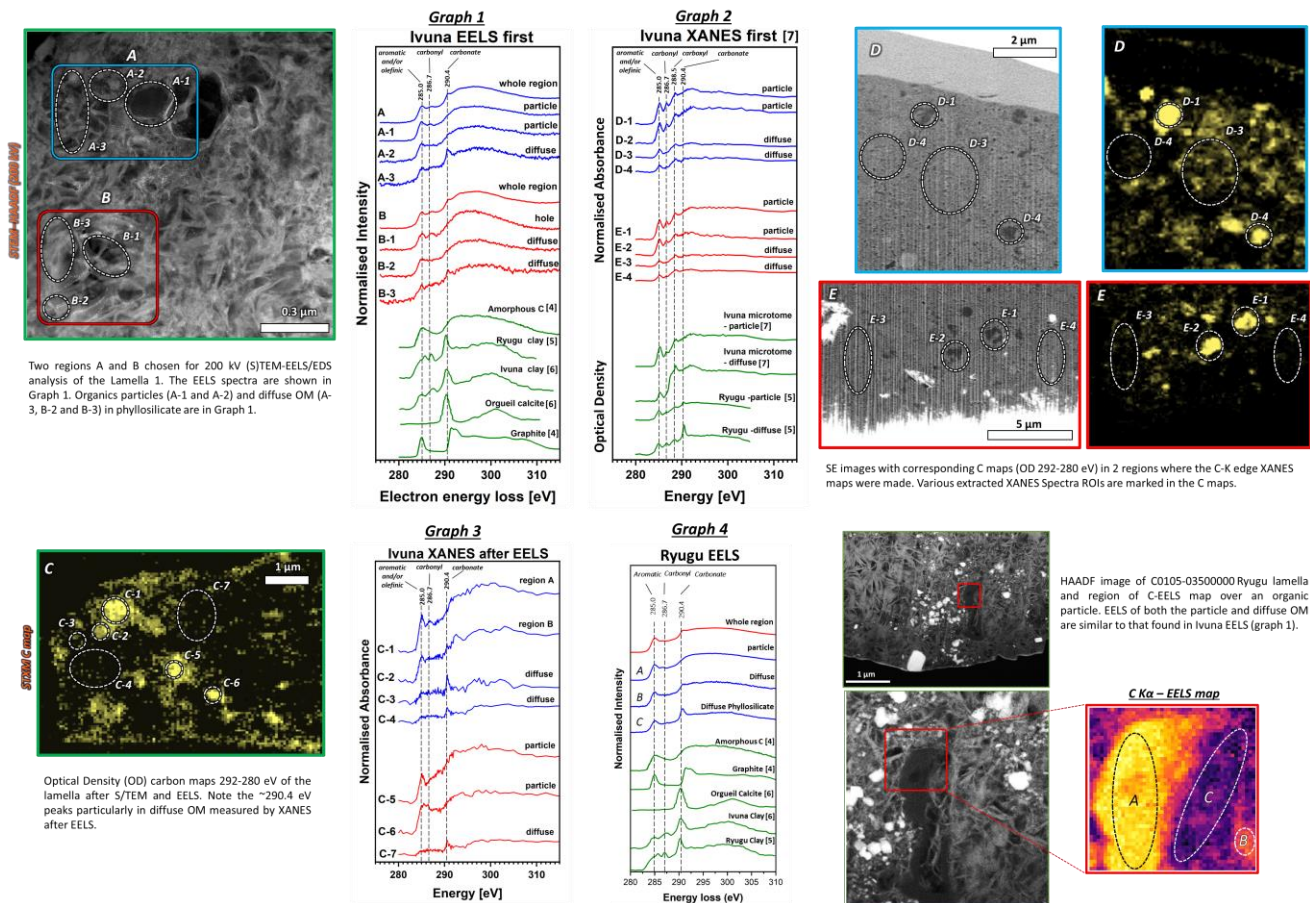


Figure 2. Carbon-EELS and -XANES on the Ivuna lamella and Ryugu sample.

Discussion The amount of radiation damage has been shown much lower in STXM-based XANES spectroscopy than in TEM-based EELS [8]. Our observations particularly of organo-carbonate bonding in diffuse OM shows its formation sensitive to e-beam exposure rather than X-ray exposure. This was also identified by [9] in terrestrial coals imaged with 5KV SEM during FIB lamella preparation. Furthermore, Yabuta et al. 2023 [5] reported the lack of any carbonate peak in microtome samples measured by XANES, but occurring in FIB sections with organic particles and diffuse OM in Ryugu samples (referred to as clay bound OM in their study). Our microtome samples of CI chips also lack this peak in any XANES measurements, suggesting that e-beam exposure during FIB-SEM preparation also formed the organo-carbonate bonds observed in previous STXM studies [e.g. 10] and recently in [5]. However, potential mixture of indigenous organo-carbonate cannot be ruled out.

Conclusions Chondritic OM is sensitive to electron radiolysis particularly by the formation of organo-carbonate bonding, although the formation mechanism is unclear. Carbon-EELS of organic particles also convolute the 288.5 eV carboxyl peak by an amorphous bulge. This means that synchrotron XANES coordinated with subsequent TEM more accurately provides a measure of functional chemical variation of chondritic OM than EELS-TEM.

FIB-SEM lamella preparation of chondritic matrices require electron energies lower than 5KV (e.g. 1.5KV) during imaging to minimize e-beam damage by radiolysis. It is unclear though whether SEM lower than 5KV could prevent the formation of this carbonate -O-C=O-O- ~290.4 eV feature, and how other regions of C-XANES and -EELS spectra are effected.

References [1] Yada T. et al. 2014. Nature Astronomy 6:214-220. [2] Lauretta et al. 2015. Meteoritics & Planetary Science 50:834-849. [3] Noguchi et al. 2020. Life 10(8):135. [4] Yuan J. & Brown L. M. 2000. Micron 31: 515-525 [5] Yabuta H. et al. 2023 Science 679:6634. [6] Garvie and Buseck 2007. Meteoritics & Planetary Science 42(12):2111-2117. [7] Changela. H. G. et al. 2023. Abstract #2848. 54th LPSC. [8] Wang J. et al. 2009. Journal of Electron Spectroscopy and Related Phenomena 170:25-36. [9] Bassim N. et al. 2012. Journal of Microscopy 245:288-301. [10] Changela. H. G. et al. (2018) Meteoritics & Planetary Science 53:1006-1029.

Acknowledgements Special thanks to the Hayabusa-2 preliminary examination SAND team for useful discussions and access to Ryugu sample C0105-03500000 in this study. We thank Diamond Light Source and electron Physical Imaging Centre ePSIC (instrument EO1, proposal MG30752). We also thank TESCAN GROUP, a.s. for use of their instrumentation and Dr. Hana Tesarova for her help. We acknowledge CF CryoEM of CIISB, Instruct-CZ Centre, supported by MEYS CR (LM2023042) and European Regional Development Fund-Project UP CIISB" (No. CZ.02.1.01/0.0/0.0/18_046/0015974). We thank KEK Photon factory for use of Beamline BL 19A for STXM.

Non Destructive Analyses of (Extra-) Terrestrial Materials by Combining Digital Optical Microscopy with LIBS (Element Analyses) and Micro Raman Spectroscopy – A New Approach

V.H. Hoffmann^{1,2}, M. Junge^{1,2}, F.Hentschel², W.W. Schmahl^{1,2}, M. Kaliwoda^{1,2}

¹Department of Earth- and Environmental Sciences, University of Munich; ²Mineralogical State Collection Munich (MSM-SNSB), Munich, Germany.

In this contribution we will present a new approach for the full analyses of highly sensitive or rare, valuable (extra-) terrestrial materials. The method is nearly non-destructive and will significantly reduce the material loss or unwanted influence to the samples / particles under investigation. The approach was specifically developed for returned samples for example from asteroids (Hayabusa 1,2; Osiris Rex, and others) [1,3,4]. It allows to obtain high resolution (in x/y/z) and sensitivity mineralogical data with minimum sample modifications. All investigations can be performed in atmospheric conditions without any preparation, so directly on the samples as obtained from the various sources.

Due to the significant brecciation and very fine grained matrix / phases, experiments on primitive carbonaceous chondrites are quite complex. Many phases in these primitive space materials are extremely sensitive against (even minor, or local) heating effects, and therefore any kind of preparation (cutting/grinding etc.), specifically in terrestrial atmospheric conditions should be minimized. In order to avoid any such effects we prefer to investigate - whenever possible - naturally broken unprepared sample materials. The representativity of the data obtained on the often small amounts of available sample material was also topic of our studies: large sets of high resolution mappings in 2D/3D can help to overcome the problem of tiny samples / fragments. Our experiences from the earlier investigations on Hayabusa 1 materials (asteroid Itokawa) were highly profitable in this context [2].

(1) Digital Optical Microscopy

Up to now, the surface morphology and mineralogy of the samples is/was pre-investigated routinely by SEM whereby in most cases carbon (or other) coatings are basic requirement. Raman experiments on such samples were then impossible because coatings on rough/raw samples cannot be removed and even more serious, investigating carbon phases was also blocked. High resolution digital microscopy (Keyence VHX950F system) can completely overcome all these severe disadvantages. The technique provides full control of sample materials by pre-selection of particles/areas in 2D/3D for the Raman experiments planned exactly on the same samples as a follow-up step (3). The capabilities of our approach will be demonstrated on a selected set of meteorite samples and terrestrial equivalents. The methodology is very well suited for a fast characterization and classification of tiny samples / fragile materials such as carbonaceous chondrites or returned samples [1-5].

(2) Element Analyses by LIBS

As a next step element analyses can directly be performed with the same instrument on the pre-selected spots or particles by LIBS – LASER Induced Breakdown Spectroscopy. No vacuum, coating or pre-preparation are required which for example means no limitations to sample sizes or shapes. The short-time LASER – material interaction causes only very minor material consumption (LASER spot diameter about 10 microns). Within few seconds the element spectra can be obtained for a large number of elements.

(3) Micro Raman Spectroscopy

Finally the samples or particles under investigation can be transferred to our Micro Raman Spectrometer. As a last step of our approach, a large number of Raman spectra can be obtained by high resolution mapping of the pre-selected spots or particles. We use a Horiba Jobin Yvon Micro Raman Spectrometer (XploRa One) at the Mineralogical State Collection Munich (MSM) for our experiments which is best suited for investigating non-prepared surfaces - to avoid any influence on preparation-sensitive extraterrestrial phases or tiny rare materials. Raman spectroscopy is a mostly non-destructive technique for systematic phase analyses specifically on very small, < 50-100 µm sized particles or even subsurface inclusions. Performing successful Micro Raman experiments on highly fragile space materials such as carbonaceous chondrites, requires the design of a highly sophisticated experimental setup to avoid or at least minimize alteration effects already during the measurements on the one hand and to guarantee a reasonable signal/noise relation on the other.

Further details and a set of examples will be provided by our iposter contribution.

Acknowledgements

We highly appreciate the support of Th. Koch from Keyence Germany GmbH, specifically concerning the application and detailed test of LIBS on a set of our samples.

References

- [1] <https://www.isas.jaxa.jp/en/missions/spacecraft/past/hayabusa.html>
- [2] Mikouchi T. and Hayabusa Consortium, 2014. Earth, Planets and Space, 66/82, 9pp
- [3] <https://mars.nasa.gov/mars2020/>
- [4] https://www.esa.int/Science_Exploration/Human_and_Robotic_Exploration/Exploration/ExoMars
- [5] Meteoritical Bulletin Database, 09/2023.

Study on Similar Continued Organic Life Systems on the Rocks of Water Planet Earth

Yasunori MIURA

Department of Earth System Sciences, Faculty of Science, Yamaguchi University

Introduction: Solid rock (mixed to pure Si, Ca, or Fe groups) system of active Earth as A3MS are different with rocky solid (mixed Si, Ca, or Fe groups) system of inactive Asteroids and the Moon as IMS, shown other paper in this volume [1]. However, organic compounds to life system of Carbon (C) groups are light elements (C, H, O, N) with rapid reaction on higher pressure and temperature (higher PT) condition different from rocky “mineral” as slower reaction in lower pressure and temperature (low PT) condition, especially its carbon behaviors as unclear sources and existence between rocks and air-fluid mixtures. Therefore, there are many unsolved problems of 1) condition (higher to lower PT) to form organic compounds (single to higher molecules), 2) carbon-bearing rocks on natural rocks formation of active Earth plane and inactive Asteroids, and 3) Artificial sources of carbon-bearing grains to be mixed with inactive Asteroids and active Earth rocks. The main purpose of the paper is to make sure origin and sources organic carbon formation on active Earth form called as Active Three Material States (A3MS) where almost products might be mixed with carbon during heating on global and local sites of active and inactive planet. [1-3] (Table 1).

Formation of organic molecules from two molecules during higher PT on inactive Asteroids: Mixed rocks with light elements including carbon rapidly cooled from air and fluid after various impacts are lightly connected with rocky grains of Si-system, where it is difficult to observed carbon-fixed to rocky Si system grains (except analytical -electron micrography) [5].

Although the carbon-bearing grains and molecules are formed easily on active water planet Earth as A3MS system, it's difficult to be formed and maintained for these grains and molecules for organic compounds because there is no closed system on airless Asteroids and the Moon even in higher PT events (by collisions *etc.*) by evaporated or quenched inorganic grains. This is the major difference with active water-planet Earth for its formation and remained sure to closed system as a A3MS system. This suggests that there are no static molecules of pure water or carbon dioxide (to make static organic molecules) at lower temperature on airless Asteroids and the Moon (except increases processes to make original two molecules continuously on inactive body).

However, carbon-bearing rocky grains are formed as quenched inorganic grains and might be formed fluid or vapor stated at increased higher PT condition even in inactive celestial bodies of an Asteroids. [4,6]

Possible man-made sources of terrestrial carbons on in active celestial bodies: If we might use any metallic products formed by normal industrial sites with higher temperature (as *ca.* 0.2 to 6.5wt.% CO₂ contents in steel materials generally), it might be leaked in inactive celestial bodies of an Asteroids and the Moon (as in impacted sample collections or cratering).

Possible cases of the formation of organic compounds from fluids and carbon dioxides on inactive celestial bodies: On inactive Asteroids and the Moon, light element CHO-system groups are easily formed from products contained carbon elements (*cf.* steel parts) with impacted sample collections and/or analytical procedures by collision less-shock wave reactions by electron, ion and laser beam bombardments in analytical chambers and inactive celestial bodies (by natural beams from Universe and the Sun) are expected carefully to be interpreted on the paper [6]. In short, various mixed aggregates can be observed in many parts of the Asteroids with carbon-bearing grains before forming the Moon or Mars planet as intermediate solid-aggregated rocks before forming the water planet Earth with other active life-A3MS system groups as a carbon-shifted system.

Table.1 Comparison of probable organic materials of Earth, Asteroids and other extraterrestrial bodies.

Celestial bodies	Carbon-bearing organic compounds	Organic Life System
Earth (water planet)	Active three material states (A3MS) system	Yes. Non-mineral elements system separated
Asteroids, the Moon (Mars)	Inactive material state (IMS), Sputtering	? Exist as carbon-bearing grains (mixture)

Summary: The present work has been summarized as follows.

- (1) Active planet model A3MS can be formed organic compounds and pure air gas and liquids.
- (2) Possible man-made sources of terrestrial carbons on in active celestial bodies.
- (3) Possible cases of the formation of organic compounds from fluids and carbon dioxides on inactive bodies are existed.

References: [1] Miura Y. (2018) IMA-22,1189. [2] Miura Y. (2023) JAMS. E5-15. [3] Miura Y. (1996) Shock-Wave Handbook (SV, Tokyo),1073-1209. [4] Miura Y. and Kato T. (1993) AIP, 283, 488-492. [5] Miura Y. (1992) Celestial Mechanic. & Dynamical Astro. (KA), 54, 249-253. [6] Y. Miura (2023) In this volume.